Master's thesis

NTNU
Norwegian University of Science and Technology
Faculty of Information Technology and Electrical Engineering
Department of Engineering Cybernetics

Morten Lie

Heave Compensated Tripping

Master's thesis in Cybernetics and Robotics
Supervisor: Ole Morten Aamo
June 2019

NTNU
Norwegian University of
Science and Technology

Morten Lie

Heave Compensated Tripping

Master's thesis in Cybernetics and Robotics
Supervisor: Ole Morten Aamo
June 2019

Norwegian University of Science and Technology
Faculty of Information Technology and Electrical Engineering
Department of Engineering Cybernetics

NTNU
Norges teknisk-naturvitenskapelige universitet

Fakultet for informasjonsteknologi og elektroteknikk

Institutt for teknisk kybernetikk

HOVEDOPPGAVE

Kandidatens navn: Morten Lie

Fag: Teknisk Kybernetikk

Oppgavens tittel: Heave compensated tripping

Bakgrunn

When drilling, the hoisting is heave compensated to ensure steady drilling with a constant weight on bit even when the floating rig is moving up and down with the waves. When tripping, that is pulling the drillstring out of the hole/lowering into the hole, the heave compensation system is not used, with the result of surge/swab effects downhole causing pressure variations and potential influxes or losses. The objective of this project work is to design a control system that isolates the string movement from rig heave, so that tripping can be performed smoothly without significant downhole pressure oscillations, and to optimize tripping velocity. The followings tasks should be addressed by the student:

1. Review the hoisting system and describe how it works today, and state-of-the art in heave compensation systems. Material from your project work can be used freely but must be cited appropriately.
2. Derive a model of the topside system from input signal to the motor to the interface with the string dynamics (i.e velocity of string and stress of string at the top). This will involve dynamics of the motor, hoisting system and heave compensation system. Justify the level of detail in the various components in the model.
3. Incorporate the model into the MATLAB drilling simulator containing the string dynamics, and run simulations to demonstrate the behavior of the added features of the simulator.
4. Continue the development of motor control strategies from your project work and compare performance (in terms of downhole pressure oscillations) for the cases {constant hoisting, heave compensation off}, {constant hoisting, heave compensation on}, {controlled hoisting, heave compensation off}.
5. If time permits: Propose an estimation strategy for the heave motion of the rig, and implement this in the control design.
6. Write report.

Faglærer/Veileder: Professor Ole Morten Aamo

Abstract

The oil and gas industry are facing numerous challenges when drilling new wells from floating vessels. One of these challenges is pressure oscillations induced in the well hole by movement of the drilling equipment. Since the relative position of a floating drilling rig to the seabed is influenced by waves, these motions may induce pressure waves in the well hole. Pressure waves with sufficient amplitude may result in fracking of the formation in the reservoir, rendering damage to the structural integrity of the well. Furthermore, during hoisting operations of the drilling equipment, these wave-induced motions are not compensated for on drilling rigs today, thus limiting the drilling operations to particular sea states.

This thesis proposes a control strategy that utilizes the hoisting system to isolate the movement of the drilling equipment from the wave-induced motion of the rig during hoisting operations. A mathematical model of a conventional hoisting system is derived and simulated together with a model describing the dynamics in the well. The analysis based on simulations presented in this work suggest combining conventional pressure control used on modern drilling rigs with active hoisting. In the simulations where the sea state was configured based on data from the North sea, the pressure oscillations were reduced by a factor of six when comparing the proposed control system with the conventional tripping method. Achieving such results in practice will reduce weather related down time, and increase safety on the platform.

Sammendrag

Olje- og gassindustrien blir møtt med store utfordringer når nye brønner skal bores fra flytende plattformer. En av disse utfordringene er trykkvariasjoner i brønnen forårsaket av bevegelse av boreutstyret. Siden havbølger har innflytelse på den relative posisjonen til en flytende borerigg i forhold til havbunnen, kan slike bølgebevegelser indusere trykkbølger nede i borehullet. Trykkbølger med tilstrekkelig styrke kan resultere i hydraulisk frakturering av formasjonen i reservoaret, som videre kan resultere i uønskede lekkasjer. Ved heising av boreutstyr blir ikke slike bølgeskapte bevegelser kompensert for på borerigger i dag. Dette begrenser boreoperasjoner til bestemte sjøganger.

Denne avhandlingen beskriver en kontrollstrategi som bruker heisesystemet til å isolere bevegelsene av boreutstyret fra de bølgeskapte bevegelsene boreriggen utsettes for under heiseoperasjoner. En matematisk modell av et konvensjonelt heisesystem er utledet og simulert sammen med en modell som beskriver dynamikken i brønnen. Analyser basert på simuleringer beskrevet i denne rapporten viser at konvensjonell trykkregulering av brønn som brukes på borerigger i dag, kombinert med aktiv kompensering for hivbevegelse under heising, gir en reduksjon av trykkbølger med en faktor på seks. Ved å oppnå slike resultater vil man i praksis kunne redusere nedetid på grunn av vær, samt øke sikkerheten på plattformen.

Preface

This master thesis was submitted as the final project required for a M.Sc. degree within the field of Cybernetics and Robotics at the Norwegian University of Science and Technology (NTNU).

The thesis was written for the Department of Engineering Cybernetics at NTNU. This work is a continuation of the author's specialization project conducted during the fall semester of 2018. The department supplied all necessary equipment, software, and a work station to complete the project. In addition, a Matlab simulator for the dynamics in a drill string and well was supplied. The simulator was developed by Timm Strecker at the Department of Engineering Cybernetics.

First and foremost, I would like to acknowledge my gratitude towards my supervisor, Professor Ole Morten Aamo at the Department of Engineering Cybernetics for an interesting assignment, and for his excellent guidance throughout the course of this work. Further, I would like to thank John-Morten Godhavn at Equinor, Martin Kvernland at Heavelock, and Timm Strecker for setting aside time to answer my questions regarding the project.

I would also like to express my gratitude towards my parents, Sverre R. Lie and Kristin R. Lie, for their love and support throughout my five years of study. In addition, I would like to thank my brother, Magnus Lie, for leading the way into the realm of engineering, and my sister, Julie Lie, for her time spent on corrective reading this thesis. Lastly, I thank my grandfather, Egil Torodd Lie, for influencing my choice of becoming an engineer, and for all the encouragement along the way.

Trondheim, June, 2019
Morten Lie

Table of Contents

List of Figures

List of Tables

Nomenclature

Greek letters

β	Bulk modulus, Pa
η	Standard deviation of noise
γ	Velocity conversion coefficient
λ	Mass per unit length, kg/m
μ	Kinematic friction coefficient
ω	Angular velocity, rad/s
ψ	Sheave velocity coefficient
ρ	Density, kg/m^3
σ	Drill string stress, Pa
θ	Inclination, rad
Ξ	Non-conservative force, N

Latin letters

A	Cross section area, m^2
E	Young's modulus, Pa
g	Gravitational acceleration, m/s^2
L	Length, m
m	Mass, kg
p	Pressure, Pa
q	Flow rate, m^3/s
r	Radius, m

T	Kinetic energy, J
t	Time, s
U	Potential energy, J
v	Velocity, m/s
z	Axial position, m

Subscripts

a	Mud in annulus
bb	Below bit
c	Crown block
d	Drum
dl	Drilling line
ds	Drill string stand
dw	Drawworks
em	Electromagnetic
fb	Feedback
ff	Feed forward
g	Gear
hb	Herschel-Bulkley
hf	Heave filter
hl	Hook load
i	Mud inside the drill string
lp	Low pass
m	Motor
mp	Mud pump
r	Reference
s	Sheave
sb	Sheave bearing
t	Travelling block
vf	Viscous friction
w	Well

wt	Water table
atm	Atmospheric pressure, 100 kPa
BHA	Bottom hole assembly
TFA	Total flow area

Superscripts

$*$	Fourier transform
$\cdot$	Derivative with respect to time
$\rightarrow$	Vector
$\tilde{}$	Error
$\top$	Transpose of a vector or matrix
$\hat{}$	Unit vector, Estimate

Chapter 1

Introduction

1.1 Background and motivation

When drilling an oil or gas well from a floating rig, a drill string with a drill bit at the end is used to access the reservoir located beneath the sea bed. During a drilling operation, the vertical movement of the rig, caused by waves, is compensated for in order to maintain a constant weight on the drill bit. However, when the drill string is hoisted up or down by the hoisting system on the rig, known as tripping, the existing compensation systems are not working effectively. As a result, the movement of the rig is propagating along the drill string, inducing a heave motion of the drill bit. According to Burkhardt [2], this vertical heave motion causes a viscous drag, resulting in pressure variations in the bottom of the well. Surge and swab effects may damage the structural integrity of the well, resulting in potential influxes or losses if the pressure exceeds the pore or fracture pressure. Wells with tight pressure margins between pore and fracture pressure can be problematic to operate under rough sea states.

This challenge has been subject to research for years. Managed pressure

drilling (MPD) is a hot topic in this research, where drilling mud is injected into the well for pressure control. As done by Breyholtz et al. [3], and Nygaard et al. [4], amongst others, the pressure down hole is controlled by a set of pumps and valves located at the topside of the well during the drilling operations. These control strategies are mainly using the down hole pressure measurements to minimize the pressure variations. However, since the location of these actuators may be relatively far away from down hole, e.g. several thousand meters, there is a significant time delay which reduces the performance of the controllers. Since the heave motion induced by the waves is a stochastic measure, it is difficult to implement model predictive controllers with sufficient prediction horizon to accommodate this time delay. Furthermore, predictive strategies rely on high precision models of the fluid dynamics down hole. Another method, as discussed in Strecker et al. [5], reduces pressure oscillations by adding acceleration instrumentation and a control valve above the bottom hole assembly. This augmentation reduces the time delay significantly. However, this method is not very effective during tripping.

The contribution of this work is to develop an active heave compensation system which utilizes the hoisting system during tripping. The task is to control the hoisting system to isolate the drill string from the heave movements of the rig, which in turn will minimize the pressure variations down hole. A typical hoisting system installed on modern rigs will be reviewed in detail, and analyzed from a physics point of view. This analysis will further be used to develop a model of the dynamics in the hoisting system, which will be implemented in a simulator using Matlab. This simulator will then be coupled with a high-fidelity model of the well dynamics and elastic drill string, developed by Strecker et al. [6], in order to simulate realistic tripping operations in different sea states. Furthermore, this hoisting system model will be used as a frame work for the development of a heave compensation control strategy for tripping.

No prior research on the topic of heave compensated tripping was found, nor any work on a dynamic model of a hoisting system. Thus, most of the derivations in this work is original, with inspiration from studies regarding MPD and steady state models of hoisting systems. These studies has been cited appropriately as the different topics are discussed in the report.

An overview of the system is given in Figure 1.1.

1.2 Outline

This report is divided into several chapters. First, an overview of a modern hoisting system will be reviewed and modelled in chapter 2. Then, in chapter 3, the drill string and well model will be described. A set of simulations will be performed in chapter 4 for validation of the models, both individually and coupled. A control strategy for heave compensation will be derived in chapter 5, before the acquisition of the necessary measurements will be described in chapter 6. Chapter 7 will present several tripping simulations, which are further discussed in chapter 8. Lastly, a conclusion of this work is drawn in chapter 9 with suggestions to future work in chapter 10.

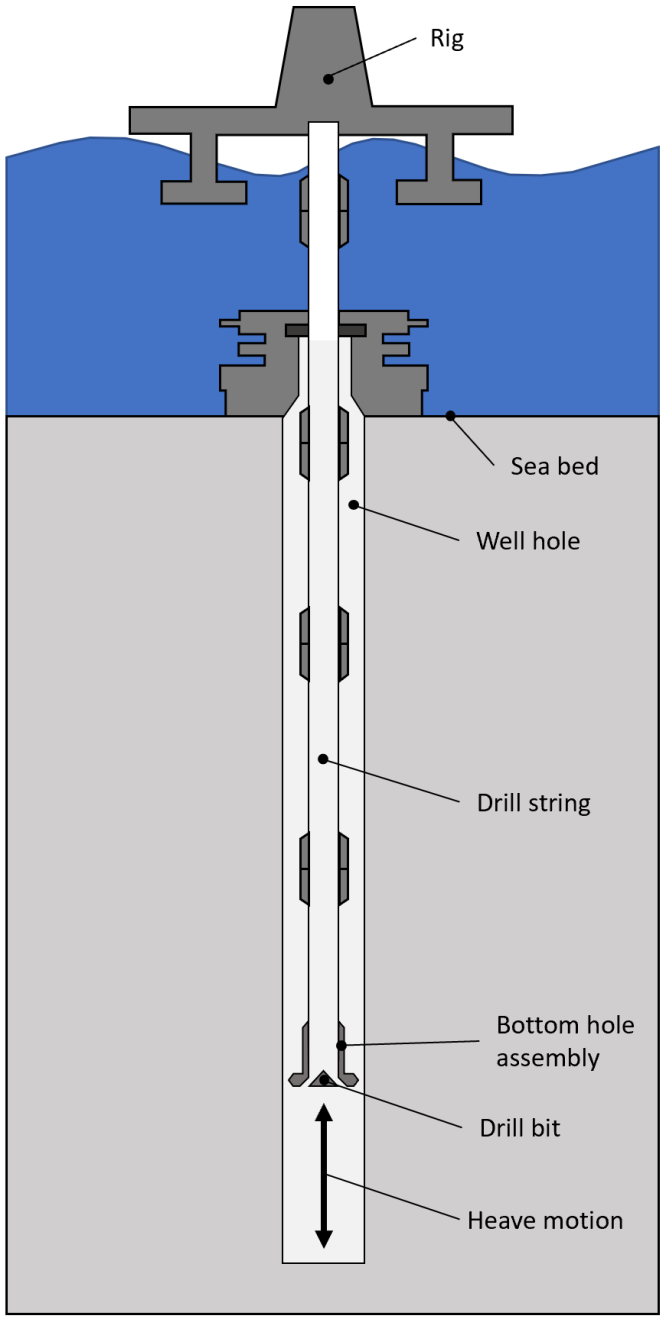

Figure 1.1: Overview of a floating rig with a drill string submerged in a well.

Chapter 2

Hoisting system

The hoisting system is one of the main components of a modern drilling rig, and is used to maneuver the drill string inside the well. In addition, the hoisting system is used to control the applied force to the drill bit. It is common for an oil or gas reservoir to be located several thousand meters below the seabed. To access the reservoir, it is common to drill vertically to a certain depth, and continue drilling horizontally through the reservoir. Therefore, the hoisting system must be able to handle drill strings of significant lengths. The drill string increases in length as new drill string segments are attached and lowered. The drill string segment is commonly known as a stand, and different mechanisms are used to feed the hoisting system with new stands. The new stand is coupled with the rest of the drill string while the drill string is locked to the rig. This locking mechanism is called slips, and one often refers to a locked drill string as *in slips*. When the stand is attached to the rest of the drill string, the hoisting system continues lowering the drill string.

According to Cayeux et al. [7], there are mainly three types of hoisting systems that are used on modern drilling rigs.

- The drawwork hoisting system where the lifting force is amplified through a block and tackle mechanism.
- The ram-rig where the lifting power is supplied by hydraulic cylinders.
- The rack and pinion rig where the lifting power is generated by converting rotational motion of a pinion into a linear motion by a rack gear.

The hoisting system that is used on most drilling rigs today is based on a block and tackle system. Thus, this work will focus on the drawwork hoisting system. In the forthcoming sections, the working principle of the drawwork hoisting system will be explained, the main components will be discussed, and a mathematical model of the drawwork will be derived. The model will be derived in order to run simulations of the hoisting system, as well as establishing a framework for a control design for heave compensation during tripping.

2.1 Drawwork

The drawwork hosting system utilizes the block and tackle principle in order to amplify the necessary lifting force to maneuver the drill string. The principle is obtained by reeving a set of sheaves between a block and a tackle with a wire, as indicated in Figure 2.1. The augmented pulling force comes at the cost of a reduced pulling speed, and an increase of friction.

The block and tackle principle is achieved in the drawwork by a crown block and a travelling block. An illustration of the drawwork can be viewed in Figure 2.2. The crown block is mounted to the water table, located at the top of the derrick. The travelling block, as the name suggests, travels up and

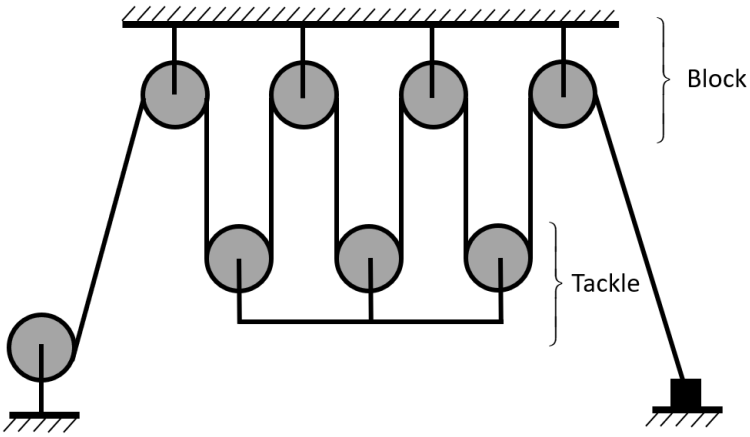

Figure 2.1: Block and tackle setup.

down inside the derrick, maneuvering the drill string. The travelling block is attached to the top drive, which is used to rotate the drill string.

The wire that runs between the blocks is called the drilling line, where one end is mounted to an anchor, and the other end is spooled onto a wire drum. The drilling line is typically divided into three sections; the dead line, the working lines and the fast line. The dead line is the section of the drilling line from the last sheave in the crown block to the anchor. The dead line is stationary, independent of the velocity of the travelling block. The working lines are composed of all the drilling line pairs that runs between the crown block and the travelling block. Note that the velocity of the working lines decreases for every turn around the travelling block, such that the working line closest to the dead line is only moving at the velocity of the travelling block. The fast line is the section of the drilling line from the wire drum to the first sheave on the crown block. If one assume there is no friction in the system, the amplification of the lifting force applied on the travelling block by the system is equal to the number of working line pairs. Thus, by increasing the number of line pairs in the configuration, the greater is the output force. However, since every sheave has a source

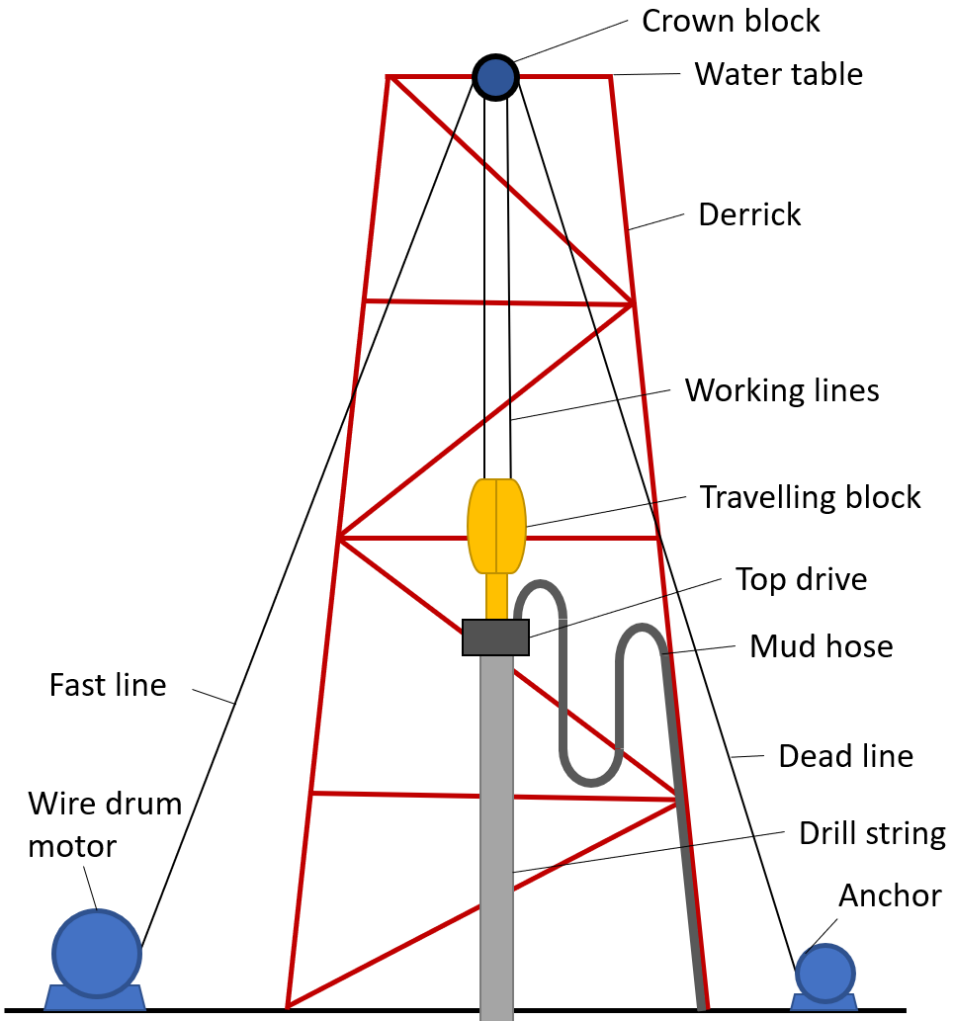

Figure 2.2: Overview of components on a drawwork hoisting system.

of contact friction with its bearing, an increase of working line will also increase the total friction in the system. Furthermore, the necessary velocity of the fast line for a given travelling block velocity increases by the number of working line pairs in the setup. According to National Oilwell [8], whom are manufactures of drawwork hoisting systems, the most common number of working line pairs in a drawwork hoisting system ranges from 8 to 12 pairs.

Further, the fast line is spooled onto a wire drum, which is driven by a motor. Both electrical and hydraulic motors are commonly used, together with gears, a drum clutch and breaks. The gears are used to allow the motor to rotate at near nominal rate. The drum clutch can be used to switch the drum between a low and high speed mode, and the breaks are used together with the motor to control the rotational velocity of the drum.

When drilling, the mud fluid is supplied by a mud pump through a mud hose, which is attached at the top of the drill string. The drill string is transporting mud fluid down hole in order to cool the drill bit, and to extract drilling debris from the well.

The load force that is exerted on the travelling block is called the hook load. The hook load is an important measure both during drilling operations, and during tripping operations, as it is used to estimate the operational conditions down hole. For instance, during drilling of a new well, the weight on bit is critical in order to achieve a successful drilling. Thus, the control systems on the rig are depending on an estimation of the hook load. The control system that will be discussed in this work is also utilizing hook load measurements. Details on how this measurement is obtained will be further discussed in chapter 6.

2.2 Drawwork model

In order to simulate a tripping operation, a model of the hoisting system is needed. A mathematical model of the drawwork will also establish a framework in which a heave compensation controller can be designed. This will be covered in chapter 5. In order to derive a representative model for the hoisting system, the main components of the drawwork will be discussed from a physics point of view. The forces that are present in the components will be presented, and the equations of motion will be derived by the end of this section. The main assumptions and model simplifications that are made will be discussed as the physical behaviors are addressed, with a summary at the end of the section.

2.2.1 Drawwork motor

The motor in the drawwork hoisting system supplies the wire drum with rotational energy through a set of gears. Both hydraulic and electric motors are used, but this work will be focusing on the electric motor. In order to model the electric motor, the direct current (DC) motor will be analyzed as it has a simpler design than the alternating current (AC) motor. According to National Oilwell Varco, a manufacturer of the drawwork hoisting system, there are always more than one motor supplying the wire drum. The drawwork is designed in this way both to increase the hoisting capacity, and to maintain a high level of redundancy.

In order to model the DC motor, one must be familiar with the key components that makes up the motor. As indicated in Figure 2.3, the key components of the motor are the commutator, the armature winding, and the permanent magnets. Suppose that the initial orientation of the rotor is as indicated in Figure 2.3a. By supplying the motor with direct current, the

commutator will direct the current onto the armature winding as indicated. Due to the flow of current through a magnetic field, an electromagnetic force called the Lorentz force is induced perpendicular to the magnetic field. This force, indicated in the figure as F_{em}, exerts a torque on the rotor. Since the force is perpendicular to the magnetic field, the torque decreases until the rotor has turned 90 degrees. At this point, the commutator directs the current in the opposite direction, such that the induced torque maintains its direction. Now, suppose that there are several armature windings in the rotor, each shifted by a certain angle from each other. This will ensure a constant torque on the rotor as long as the motor is supplied with a direct current.

The dynamics of the motor can be explored by modelling the inductive- and resistive properties of the armature windings. Consider the RL circuit in Figure 2.4. The resistor and inductor encapsulates the electric resistance and inductance in the armature windings, respectively. Since the armature windings are rotating in the magnetic field created by the permanent magnets, a voltage is induced in the windings. This voltage is back-supplied to the armature winding due to the rotation of the windings in a magnetic field, and is denoted the back emf voltage. It can be shown that the magnitude of this voltage is proportional to the rotational velocity of the rotor. Mathematically, it can be expressed as

$$e_a = K_v \omega_m, \tag{2.1}$$

where e_a is the back emf voltage, K_v is a proportionality constant, and ω_m is the rotational velocity of the motor.

By applying Kirchhoff's 2$^{\text{nd}}$ law to the circuit in Figure 2.4, which states that the sum of all the voltage supplies and the voltage drops in a closed circuit will equal zero, the dynamics of the electric circuit can be exploited. By Ohms law, the voltage drop over the resistor is proportional to the ar-

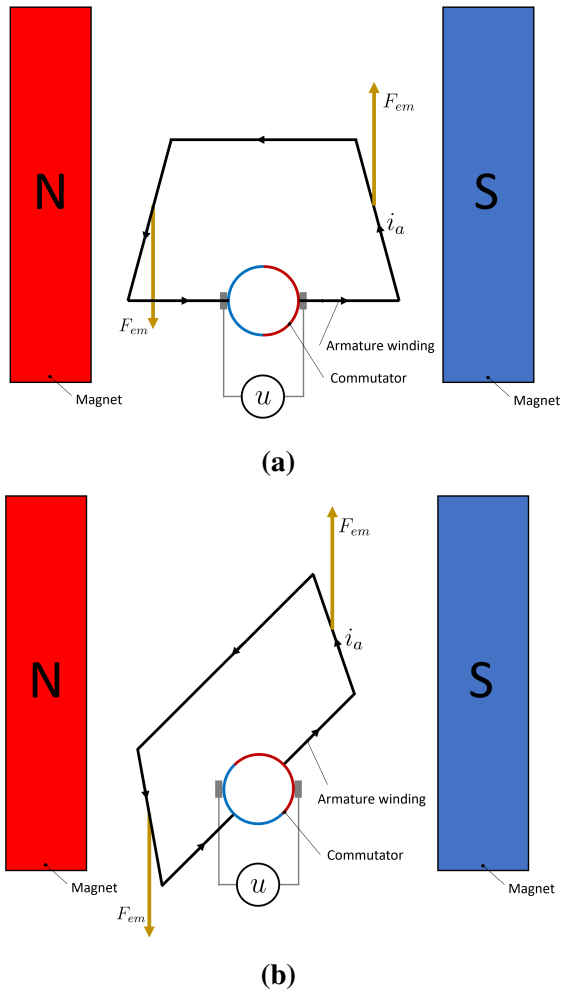

Figure 2.3: Working principle of the DC motor.

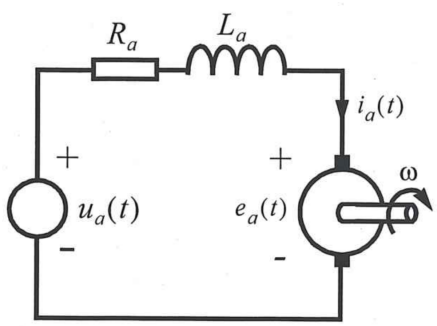

Figure 2.4: RL circuit of the armature winding in a DC motor, adapted from [1].

mature current, i_a. Mathematically, the voltage drop, V_R, can be expressed as

$$V_R = R_a i_a. \tag{2.2}$$

Further, the voltage drop over the inductor is proportional to the rate of change of the armature current with respect to time. Denoting the voltage drop over the inductor as V_L, the voltage drop can be expressed as

$$V_L = L_a \frac{di_a}{dt}. \tag{2.3}$$

Kirchhoff's 2nd law yields the following expression.

$$\begin{aligned} u_a - V_R - V_L + e_a &= 0 \\ u_a - R_a i_a - L_a \frac{di_a}{dt} + e_a &= 0 \end{aligned} \tag{2.4}$$

By inserting the back emf expression in Equation (2.1), and solving the equation for the time derivative of the armature current, the dynamics of the current in the armature windings is expressed as follows.

$$\frac{di_a}{dt} = \frac{1}{L_a}(u - K_v \omega_m - R_a i_a) \tag{2.5}$$

Next, the mechanical dynamics of the motor will be investigated. The elec-

tromagnetic torque induced in the motor is proportional to the armature current in the rotor, expressed as

$$\tau_{em} = K_t i_a, \tag{2.6}$$

where K_t is a proportionality constant. Furthermore, there is a viscous friction force exerted on the rotor. This friction is proportional to the rotational velocity of the motor, expressed as

$$\tau_{vf} = -B_a \omega_m, \tag{2.7}$$

where B_a is a friction coefficient. The total torque exerted on the rotor, which is applied to the wire drum gear, results in

$$\begin{aligned} \tau_m &= \tau_{em} + \tau_{vf}, \\ \tau_m &= K_t i_a - B_a \omega_m. \end{aligned} \tag{2.8}$$

2.2.2 Wire drum

In order to derive a complete model for the drawwork system, the moment of inertia in the wire drum must be derived. The moment of inertia is the rotational counterpart of the mass for bodies in translational movement. It depends on the mass of the body, and how the mass is distributed with respect to the axis of rotation. The mathematical definition of the moment of inertia is expressed as follows, adapted from Young et al. [9].

$$J = \sum_i m_i r_i^2 \tag{2.9}$$

Here, the total moment of inertia, J, is calculated by summing up all the point masses i that contains a mass m_i which is located at a distance r_i from

the axis of rotation.

For the wire drum, the total moment of inertia depends on the radius of the drum, as well as the number of layers that are spooled onto the drum. As discussed by Cayeux [10], and illustrated in Figure 2.5, the radial distance from the axis of rotation to the outer layer of drill line follows the relationship

$$r_d(n_l) = r_{d0} + r_{dl}\left(1 + n_l\sqrt{3}\right), \tag{2.10}$$

where r_{d0} is the radius of the empty drum, r_{dl} is the radius of the drill line and n_l is the number of layers spooled on the drum.

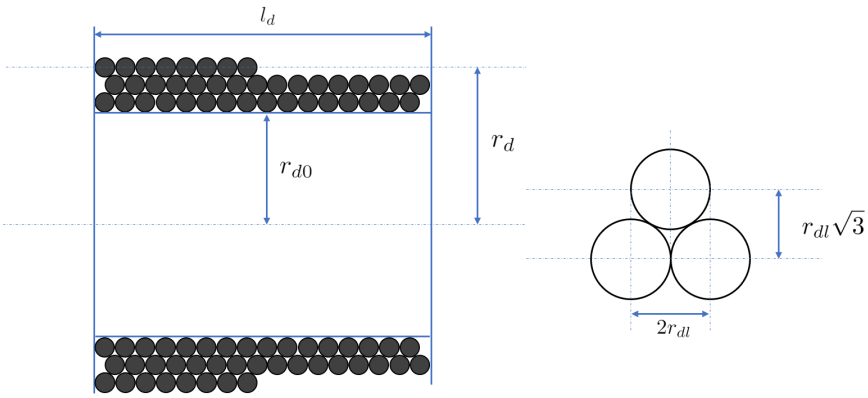

Figure 2.5: Drill line spooled onto a wire drum.

The total moment of inertia of the wire drum will be the sum of the moment of inertia of the empty drum, denoted as J_{d0}, and the layers of drill line spooled on the drum. The moment of inertia of the completed wire layers can be calculated by considering the moment of inertia of a hoop about a symmetric axis. Given a hoop of mass m and radius r, one may utilize Equation (2.9) to calculate the moment of inertia of the hoop to be

$$J_{hoop} = mr^2, \tag{2.11}$$

by observing that all the mass is distributed at the same distance r from the axis of rotation. The mass of a complete layer depends on the specific radius at which the layer got spooled onto the drum, as the radius increase for each layer. For a complete layer number i of drill line on the drum, the length of drill line on this layer can be calculated as

$$\begin{aligned} l_i &= \underbrace{2\pi r_d(i)}_{\text{Length of drill line per revolution}} \underbrace{\frac{l_d}{2r_{dl}}}_{\text{Number of revolutions per layer}} \\ &= \frac{\pi l_d}{r_{dl}} r_d(i), \end{aligned} \tag{2.12}$$

where $r_d(i)$ is the radius function in Equation (2.10), and l_d is the width of the drum. Subsequently, the mass of a complete layer i takes the form

$$\begin{aligned} m_i &= \lambda_{dl} l_i \\ &= \lambda_{dl} \frac{\pi l_d}{r_{dl}} r_d(i), \end{aligned} \tag{2.13}$$

where λ_{dl} is the mass per unit length of drill line.

Further, the final non-complete layer of drill line will also contribute to the total moment of inertia. Let l_{dld} represent the total length of drill line spooled on the drum. The length of the last, non-complete layer of drill line, can be calculated by taking the total length that is spooled onto the drum and subtracting the length of the complete layers. The length of the complete layers can be calculated by summing up the length on each complete layer, i.e.

$$\sum_{i=0}^{n_l - 1} \frac{\pi l_d}{r_{dl}} r_d(i).$$

Thus, the expression for the total moment of inertia of a wire drum with n_l

layers of drill line results in

$$J_d = \underbrace{J_{d0}}_{\text{Empty drum}} + \underbrace{\sum_{i=0}^{n_l-1} \lambda_{dl} \frac{\pi l_d}{r_{dl}} r_d(i)^3}_{\text{Complete layers of drill line}} + \underbrace{\left[l_{dld} - \sum_{i=0}^{n_l-1} \frac{\pi l_d}{r_{dl}} r_d(i) \right] \lambda_{dl} r_d(n_l)^2}_{\text{Non-complete layer of drill line}}, \tag{2.14}$$

which will be further used in the derivation of the equations of motion. One may argue that there is also a viscous friction force exerted on the wire drum. To simplify the calculations, this friction force is assumed to be governed by the friction force covered in the model for the electric motor.

2.2.3 Block and tackle system

Next, the friction forces that act on the sheaves in the block and tackle system will be examined. Since the simulations in later chapters will mainly cover tripping operations, the sheaves will be in motion throughout the simulations. Thus, this work will only consider the kinematic friction force in the sheaves.

As indicated in Figure 2.6, the sheaves are resting on an axle located in the center of the sheave. For the sheave to rotate freely in the block, a ball bearing is attached to the axle, with radius r_{sb}, which introduce a friction force exerted on the sheave. In order to model this friction force, the Coulomb friction model is utilized, given in Egeland et al. [11]. The friction model describes a force that is proportional to the normal force F_N, and has the direction opposite of the rotation of the sheave. I.e. if the sheave is rotating counter clockwise, the force will be in the positive x-direction, as indicated in the figure. By defining the positive direction of rotation to be clockwise, the friction force may be expressed as

$$\overrightarrow{F}_f = -\mu |F_N| \operatorname{sgn}(\omega) \hat{x}. \tag{2.15}$$

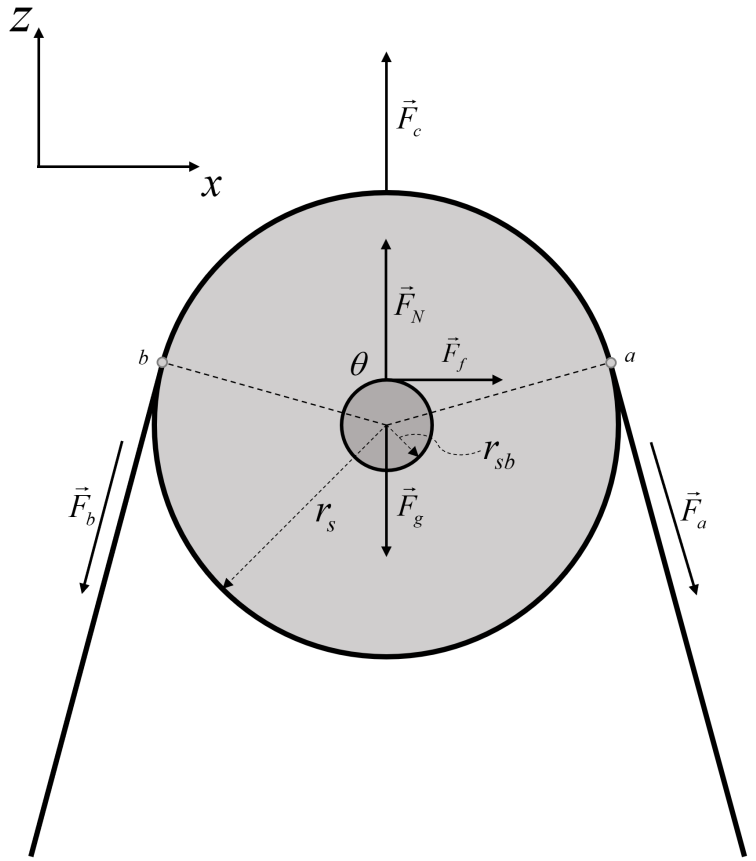

Figure 2.6: Free body diagram of a crown block sheave in the drawwork hoisting system.

Here, μ is the kinematic friction coefficient, and $\mathrm{sgn}(\omega)$ is the signum function that returns the sign of the angular velocity ω. Let μ_s be the kinematic friction coefficient in a ball bearing, the torque exerted on sheave i caused by friction takes the form

$$\tau_{f,i} = -\mu_s |F_N| r_{sb} \,\mathrm{sgn}(\omega_i). \tag{2.16}$$

For the purpose of calculating the normal force F_N, it is assumed that the sheave has no translational acceleration. Under this assumption, the normal force is equal to the sum of all the forces that are acting on the sheave along the z-axis. If one assume that the forces F_a and F_b, indicated in Figure 2.6, are parallel with the z-axis, the normal force results in

$$\overrightarrow{F}_N = \overrightarrow{F}_a + \overrightarrow{F}_b + \overrightarrow{F}_c + \overrightarrow{F}_g. \tag{2.17}$$

Here, $\overrightarrow{F}_a$ and $\overrightarrow{F}_b$ are the tension forces exerted on the sheave by the drilling line, $\overrightarrow{F}_c$ is a centrifugal force that is applied to the length of the drilling line that is changing direction by circular motion, and $\overrightarrow{F}_g$ is the gravitational force. An analysis of these forces will now be given for an arbitrary sheave in the crown block. The normal force is derived similarly for a sheave in the travelling block.

For the purpose of modelling the tension forces, $\overrightarrow{F}_a$ and $\overrightarrow{F}_b$, it is assumed that the hook load force $\overrightarrow{F}_{hl}$, is evenly distributed on each of the n_l working lines in the block and tackle setup. Under this assumption, the tension forces can be calculated as

$$\overrightarrow{F}_a = \overrightarrow{F}_b = \frac{1}{n_l}\overrightarrow{F}_{hl}. \tag{2.18}$$

As derived by Cayeux et al. [7], the centrifugal force $\overrightarrow{F}_c$ can be calculated by considering a control element of drill string of length ds moving at a

translational velocity of $v = \omega r_s$. Here, ω and r_s are the angular velocity and the outer radius of an arbitrary sheave, respectively. The acceleration of this control element can be expressed as

$$a_c = \frac{v^2}{r_s}. \tag{2.19}$$

By Newtons 2nd law of motion, the force exerted on the control element $\overrightarrow{dF}_c$, can be calculated as

$$\begin{aligned} \overrightarrow{dF}_c &= \lambda_{dl} \frac{v^2}{r_s} \hat{r} ds, \\ &= \lambda_{dl} r_s \omega^2 \hat{r} ds. \end{aligned} \tag{2.20}$$

Here, $\hat{r}$ is the unit vector in the radial direction, and λ_{dl} is the mass per unit length of drill line. The total force exerted on the drilling line as it runs over the sheave may be derived by integrating the expression in Equation (2.20) from the contact points a and b, indicated in Figure 2.6.

$$\overrightarrow{F}_c = \int_a^b \lambda_{dl} r_s \omega^2 \hat{r} ds \tag{2.21}$$

By a change of variables $ds = r_s d\theta$, and assuming that the contact points a and b are located such that the angle θ is 180 degrees, the force can be expressed in the Cartesian coordinate system.

$$\begin{aligned} \overrightarrow{F}_c &= \int_{-\frac{\theta}{2}}^{\frac{\theta}{2}} -\lambda_{dl} r_s^2 \omega^2 cos(\theta) d\theta \hat{z} \\ &= -\lambda_{dl} r_s^2 \omega^2 \int_{-\frac{\theta}{2}}^{\frac{\theta}{2}} cos(\theta) d\theta \hat{z} \\ &= -2\lambda_{dl} r_s^2 \omega^2 \hat{z}. \end{aligned} \tag{2.22}$$

Lastly, the force of gravity exerted on the sheave must be calculated. By

Newtons 2nd law, the gravitational force $\overrightarrow{F}_g$ take the form

$$\overrightarrow{F}_g = m_s g \hat{z}, \tag{2.23}$$

where m_s and g are the mass of the sheave and the gravitational acceleration, respectively.

By inserting the forces derived into Equation (2.17), the normal force exerted on an arbitrary sheave results in

$$\overrightarrow{F}_N = \left| \frac{2F_{hl}}{n_l} - 2\lambda_{dl} r_s^2 \omega^2 + m_s g \right| \hat{z}. \tag{2.24}$$

Substituting the expressions for the normal force into Equation (2.16), the friction torque exerted on sheave i may be expressed as follows.

$$\tau_{f,i} = -\mu_s r_{sb} \left| \frac{2F_{hl}}{n_l} - 2\lambda_{dl} r_s^2 \omega_i^2 + m_s g \right| \operatorname{sgn}(\omega_i) \tag{2.25}$$

For the purpose of finding the total friction torque in the block and tackle system, one has to sum all the friction torques exerted on all the sheaves that are in motion. Since the last sheave, which is next to the anchor, is stationary, the friction torque exerted on this sheave will not effect the total friction torque. Thus, the total friction torque in the block and tackle system is

$$\begin{aligned} \tau_f &= \sum_{i=1}^{n_l} \tau_{f,i}, \\ &= -\sum_{i=1}^{n_l} \left[\mu_s r_{sb} \left| \frac{2F_{hl}}{n_l} - 2\lambda_{dl} r_s^2 \omega_i^2 + m_s g \right| \operatorname{sgn}(\omega_i) \right], \end{aligned} \tag{2.26}$$

where the last sheave on the travelling block, i.e. the one closest to the anchor, is indexed n_l.

In order to derive the equations of motion later in this chapter, a common reference frame is needed for all the torques in the system. To make this intuitive, all the torques will be expressed with respect to the rotor in the electric motor. In order to transform the torques that are exerted on the sheaves in Equation (2.26) to the motor, the factor $\frac{r_d}{r_s}n_g$ must be used. Recall that r_d, r_s and n_g are the radius of the drum in Equation (2.10), the outer radius of the sheave, and the gear ratio, respectively. The friction torque from the block and tackle system exerted on the rotor of the electric motor has the following expression.

$$\begin{aligned}\tau_{f,m} &= \frac{r_d}{r_s}n_g\tau_f \\ &= -\frac{r_d}{r_s}n_g\sum_{i=1}^{n_l}\left[\mu_s r_{sb}\left|\frac{2F_{hl}}{n_l} - 2\lambda_{dl}r_s^2\omega_i^2 + m_s g\right|\operatorname{sgn}(\omega_i)\right] \end{aligned} \tag{2.27}$$

2.2.4 Crown mounted compensator

The crown mounted compensator (CMC) is a passive heave compensation device that is mounted at the top of the derrick, and is typically utilized under drilling operations. The crown block is suspended above a couple of hydraulic cylinders, allowing the movement of the crown block to follow the waves relative to the water table. Consider the illustration in Figure 2.7. The vertical movement of the crown block is counteracted by the hydraulic cylinders which are pressurized by air bottles through a separator. The greater the hook load force exerted on the crown block, the greater is the oil to gas ratio in the separator, which will increase the air pressure in the air bottles. When the hook load changes, the system converges to its new equilibrium state. This compensation system acts similarly to a spring-damper system, and will be modelled as such. Let z_c be the vertical position of the crown block, and let z_{wt} be the vertical position of the water table. By Hooke's law, the force acting on the crown block by the spring effect is

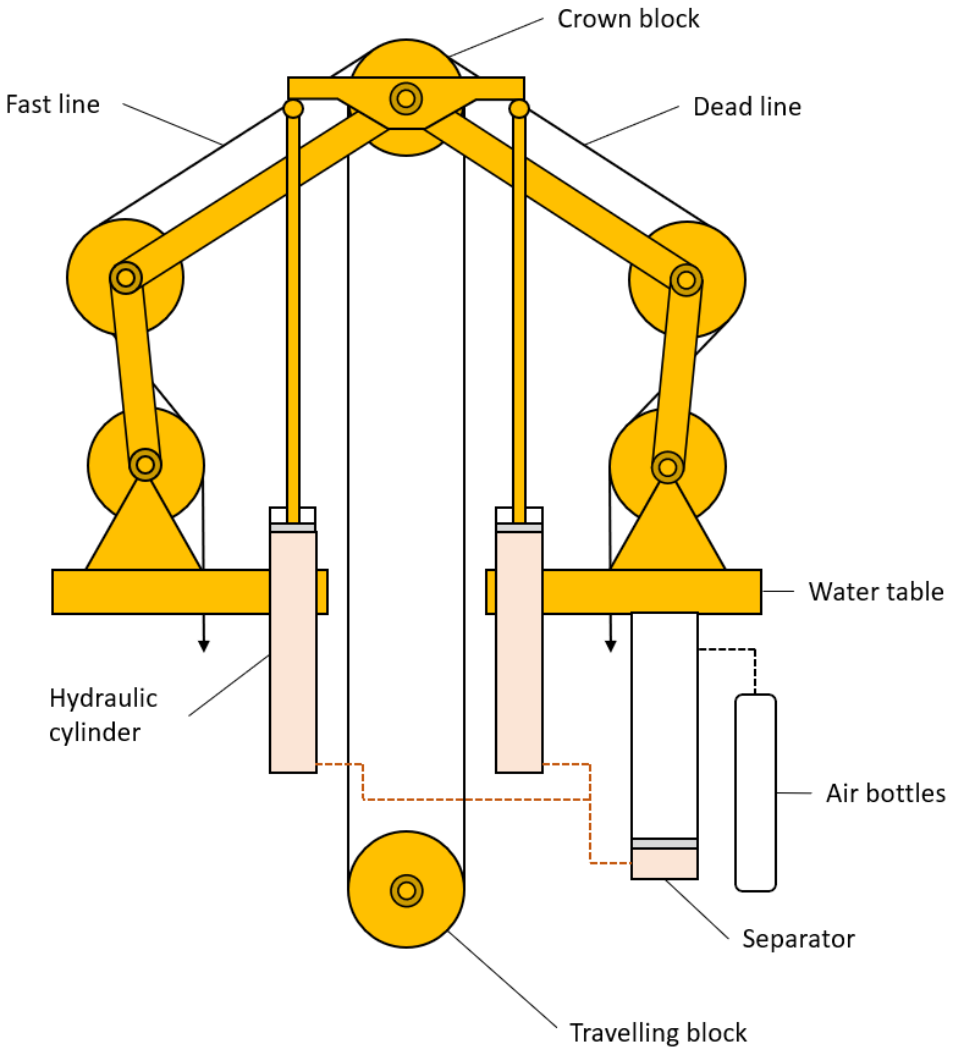

Figure 2.7: Schematic of the crown mounted compensator, manufactured by National Oilwell Varco.

proportional to the deviated position. The expression takes form

$$\overrightarrow{F}_{spring} = k_c(z_{wt} - z_c)\hat{z}, \tag{2.28}$$

where k_c is the proportionality coefficient, called the spring constant. Since the energy is not entirely conserved in the crown mounted compensator, i.e. converts to heat by friction and pressure oscillations, a mechanical damping is present. This damping force can be expressed as follows.

$$\overrightarrow{F}_{damper} = b_c(\dot{z}_{wt} - \dot{z}_c)\hat{z} \tag{2.29}$$

Here, b_c is the proportionality constant of the damper, called the damper constant. The spring force and the damper force can be adjusted by changing the pressure in the air bottles, and the number of air bottles in the setup.

2.2.5 Equations of motion

To derive the model of the complete hoisting system, Lagrange's equation of motion will be utilized, stated by Egeland et al. [11]. The equations of motion will be derived with respect to the rig reference frame. E.g. all the velocities will be relative to the drilling deck on the rig. The Lagrange's equation of motion is formulated using the *Lagrangian*, which is expressed as

$$\mathcal{L}(\boldsymbol{q}, \dot{\boldsymbol{q}}, t) = T(\boldsymbol{q}, \dot{\boldsymbol{q}}, t) - U(\boldsymbol{q}), \tag{2.30}$$

where $\boldsymbol{q}$ is the generalized coordinate vector for the model, and T and U are the kinetic and potential energy in the system, respectively. The generalized coordinates that will be used in the derivation are the angle of the motor, and the position of the crown block. I.e. $\boldsymbol{q} = [\theta_m \quad z_c]^\top$. The equation of

motion for the generalized coordinate element *i* is stated as

$$\frac{d}{dt}\left(\frac{\partial \mathcal{L}}{\partial \dot{q}_i}\right) - \frac{\partial \mathcal{L}}{\partial q_i} = \Xi_i, \tag{2.31}$$

where Ξ_i is the non-conservative force related to the i$^{\text{th}}$ generalized coordinate.

In order to derive the Lagrangian in Equation (2.30), the kinetic and potential energy of the components in the drawwork must be examined. It is assumed that the gears are massless, and have no friction. Consider the free body diagram of the drawwork illustrated in Figure 2.8, which will be the basis for the modelling.

The motor has only rotational energy, so the total kinetic energy of the drawwork motor is

$$T_m = \frac{1}{2} J_m \omega_m^2, \tag{2.32}$$

where J_m and ω_m are the moment of inertia and angular velocity of the rotor, respectively. Similarly with the wire drum, the total kinetic energy can be expressed as the following.

$$\begin{aligned} T_d &= \frac{1}{2} J_d \omega_d^2 \\ &= \frac{1}{2} J_d \left(n_g \omega_m\right)^2 \end{aligned} \tag{2.33}$$

Here, the moment of inertia J_d, is expressed in Equation (2.14), ω_d is the angular velocity of the drum, and n_g is the gear ratio.

Next, the energy in the block and tackle system will be considered. The kinetic and potential energy in the drilling line has been neglected in this work, as well as its elastic properties. As described in the previous section, the crown block is suspended in the crown mounted compensator. The CMC will be modelled as a spring damper system, where the potential en-

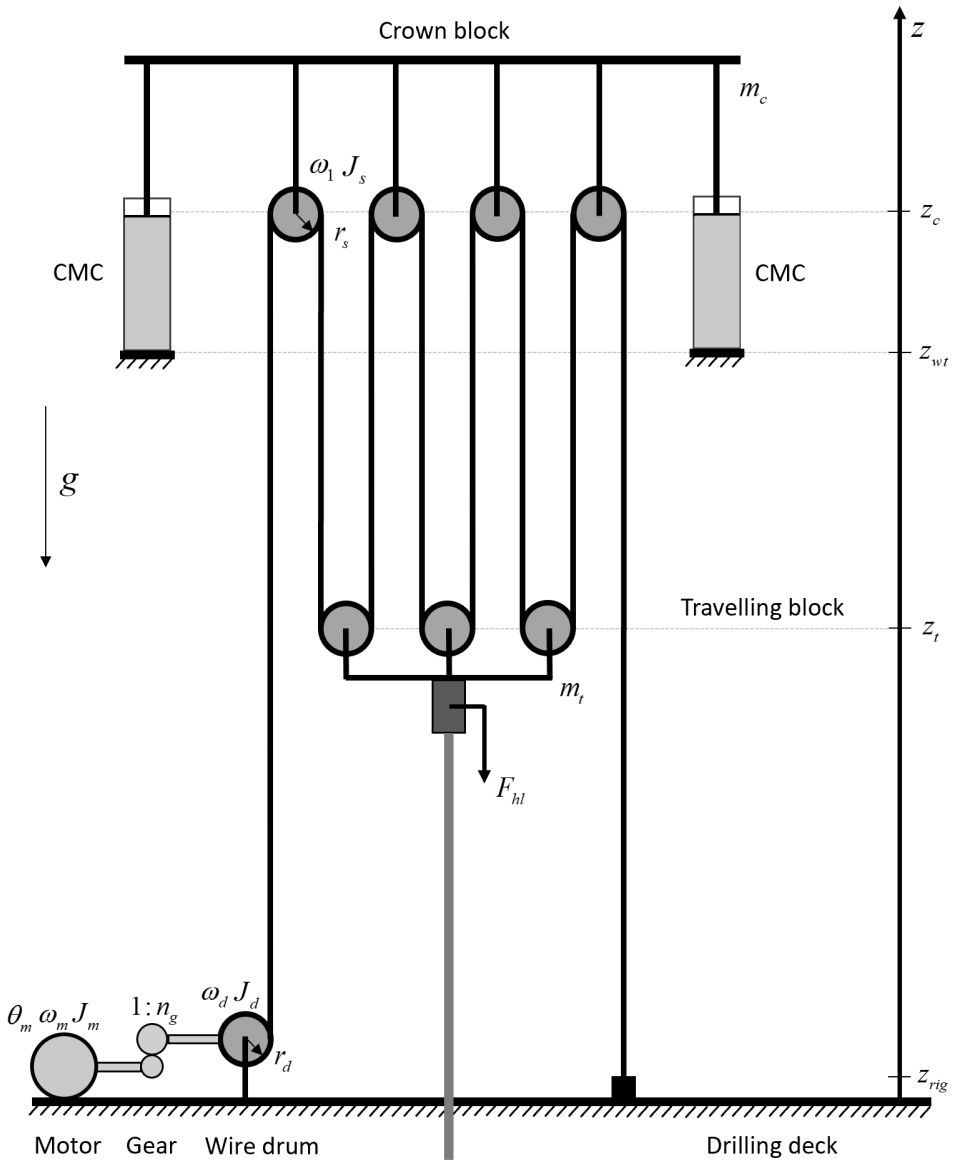

Figure 2.8: Free body diagram of the drawwork hoisting system with 6 working lines ($n_l = 6$).

ergy in the spring is stored by a deviation in the position of the crown block, relative to the initial equilibrium of the system. The damper, however, is not capable of storing energy, thus acts as a non-conservative force on the system. This non-conservative force will be taken into account on the right hand side of the Lagrangian equation of motion, stated in Equation (2.31). The potential energy stored in the spring can be calculated as follows, utilizing the spring force in Equation (2.28), and denoting $\tilde{z} = z_{wt} - z_c$.

$$\begin{aligned} U_{spring} &= \int F_{spring}(\tilde{z}) d\tilde{z} \\ &= \int k_c \tilde{z} d\tilde{z} \\ &= \frac{1}{2} k_c \tilde{z}^2 \end{aligned} \tag{2.34}$$

Here, the potential energy in the CMC is defined to be zero when $z_{wt} = z_c$.

The total potential energy in the crown block, denoted U_c, is the sum of the energy stored in the spring, and the potential energy caused by gravity, resulting in

$$U_c = \frac{1}{2} k_c (z_{wt} - z_c)^2 + m_c g z_c. \tag{2.35}$$

Here, m_c is the mass of the crown block, and g is the gravitational acceleration. In addition to the potential energy stored in the crown block, there is also kinetic energy due to the fact that the CMC gives the crown block freedom to have translational velocity relative to the rig. By denoting the kinetic energy in the crown block as T_c, it may be calculated as

$$T_c = \frac{1}{2} m_c \dot{z_c}^2. \tag{2.36}$$

In addition to the crown block, there is also energy stored in the travelling block. As with the crown block, the travelling block has potential energy

due to earths gravitational field, denoted U_t. Observe that the position of the travelling block is both a function of the angle of the motor, and the position of the crown block. Mathematically, the crown block position follows the relationship

$$z_t = \frac{2}{n_l} r_d n_g \theta_m + (z_c - z_{wt}). \tag{2.37}$$

Here, n_l is the number of working lines in the block and tackle configuration. Under this expression, the potential energy of the travelling block may be calculated as follows.

$$\begin{aligned} U_t &= m_t g z_t \\ &= m_t g \left(\frac{2}{n_l} r_d n_g \theta_m + (z_c - z_{wt}) \right) \end{aligned} \tag{2.38}$$

Since the travelling block is suspended under the crown block, the translational velocity of the travelling block will be both a function of the translational velocity of the crown block as well as the rotational velocity of the motor. Let v_t be the translational velocity of the travelling block, then the kinetic energy can be expressed as follows.

$$T_t = \frac{1}{2} m_t v_t^2 \tag{2.39}$$

Observe that the translational velocity of the travelling block can be calculated by adding the contribution of the rotational velocity of the motor, and the translational velocity of the crown block. Mathematically, this may be expressed as

$$v_t = \frac{2}{n_l} r_d n_g \omega_m + \dot{z}_c, \tag{2.40}$$

which substituted into Equation (2.39) yields

$$T_t = \frac{1}{2} m_t \left(\frac{2}{n_l} r_d n_g \omega_m + \dot{z}_c \right)^2. \tag{2.41}$$

So far, the energy related to the translational motion of the block and tackle system has been discussed. Recall that the sheaves in the crown- and travelling block are massive, such that they are able to store rotational kinetic energy. In order to model the rotational energy in the sheaves, the energy must be expressed in terms of the generalized coordinates. It can be shown that the ratio between the rotational velocity of the first sheave, and the i$^{\text{th}}$ sheave in the block and tackle configuration, can be expressed as follows.

$$\frac{\omega_i}{\omega_1} = \begin{cases} -1 + \frac{2}{n_l}\left(\frac{i}{2} - 1\right), & \text{i even} \\ 1 - \frac{2}{n_l}\left(\frac{i+1}{2} - 1\right), & \text{i odd} \end{cases} \tag{2.42}$$

The derivation of this relationship can be found in Appendix A. By considering the sheaves as solid discs with mass m_s, and outer radius r_s, the moment of inertia of a sheave can be calculated to be

$$J_s = \frac{1}{2} m_s r_s^2. \tag{2.43}$$

With the moment of inertia calculated, and the sheave velocity ratio in Equation (2.42), the rotational kinetic energy in the sheaves can be derived as follows.

$$\begin{aligned} T_s &= \sum_{i=1}^{n_l} \frac{1}{2} J_s \omega_i^2 \\ &= \frac{1}{2} J_s \underbrace{\sum_{i=1}^{n_l} \left[\begin{cases} -1 + \frac{2}{n_l}\left(\frac{i}{2} - 1\right), & \text{i even} \\ 1 - \frac{2}{n_l}\left(\frac{i+1}{2} - 1\right), & \text{i odd} \end{cases} \right]^2}_{\psi(n_l)^2} \omega_1^2 \\ &= \frac{1}{2} J_s \psi(n_l)^2 \omega_1^2 \\ &= \frac{1}{2} J_s \psi(n_l)^2 \left(\frac{r_d}{r_s} n_g \right)^2 \omega_m^2 \end{aligned} \tag{2.44}$$

Here, the assumption has been made that the angular velocity of the sheaves is only depending on the angular velocity of the motor, and not on the translational velocity of the crown block. As one may observe, by locking the angle θ_m, and increasing the vertical position of the crown block, the sheaves would indeed rotate. But since the movement of the crown block is within a few meters, and the fact that the motor is the main source of movement of the travelling block, the influence of the translational velocity of the crown block on the rotational velocity of the sheaves is neglected.

Summarizing the energy expressions derived so far, the total kinetic energy in the system can be expressed as functions of the generalized coordinates

$$\begin{aligned} T &= T_m + T_d + T_c + T_t + T_s \\ &= \underbrace{\frac{1}{2}J_m\omega_m^2}_{\text{Motor}} + \underbrace{\frac{1}{2}J_d n_g^2\omega_m^2}_{\text{Drum}} + \underbrace{\frac{1}{2}m_c\dot{z_c}^2}_{\text{Crown block}} + \ldots \\ &\quad \underbrace{\frac{1}{2}m_t\left(\frac{2}{n_l}r_d n_g\omega_m + \dot{z_c}\right)^2}_{\text{Travelling block}} + \underbrace{\frac{1}{2}J_s\psi(n_l)^2\left(\frac{r_d}{r_s}n_g\right)^2\omega_m^2}_{\text{Sheaves}}, \end{aligned} \tag{2.45}$$

and the total potential energy

$$\begin{aligned} U &= U_c + U_t \\ &= \underbrace{\frac{1}{2}k_c(z_{wt} - z_c)^2 + m_c g z_c}_{\text{Crown block}} + \underbrace{m_t g\left(\frac{2}{n_l}r_d n_g\theta_m + (z_c - z_{wt})\right)}_{\text{Travelling block}}. \end{aligned} \tag{2.46}$$

With the expressions in Equations (2.45) and (2.46), the Lagrangian in Equation (2.30) can be calculated. To simplify notation, let the total mo-

ment of inertia be denoted as J_{tot},

$$J_{tot} = J_m + J_d n_g^2 + J_s \psi(n_l)^2 \left(\frac{r_d}{r_s} n_g\right)^2, \tag{2.47}$$

and let

$$\gamma = \frac{2}{n_l} r_d n_g \tag{2.48}$$

be the conversion factor from the motors rotational velocity to the translational velocity of the travelling block. The Lagrangian takes the following form.

$$\begin{aligned} \mathcal{L} &= T - U \\ &= \frac{1}{2} J_{tot} \omega_m^2 + \frac{1}{2} m_t \left(\gamma \omega_m + \dot{z}_c\right)^2 + \frac{1}{2} m_c \dot{z}_c^2 \\ &- \frac{1}{2} k_c (z_{wt} - z_c)^2 - m_c g z_c - m_t g \left(\gamma \theta_m + (z_c - z_{wt})\right) \end{aligned} \tag{2.49}$$

Before the equations of motion can be completed, the non-conservative forces must be addressed. The first generalized coordinate is the rotor angle of the motor. The torques that are acting on the rotor are the electromagnetic torque induced by the motor itself τ_m, the torque produced by the hook load τ_{hl}, and the friction torque $\tau_{f,m}$ expressed in Equation (2.27). The second generalized coordinate is the position of the crown block. The non-conservative forces associated with the crown block is the damping force F_{damper} in Equation (2.29), and the hook load F_{hl}. The non-conservative terms in Lagrange's equation of motion results in the following.

$$\Xi_{\theta_m} = \tau_m - \tau_{hl} - \tau_{f,m} \tag{2.50}$$

$$\Xi_{z_c} = b_c(\dot{z}_{wt} - \dot{z}_c) - F_{hl} \tag{2.51}$$

Since there are two generalized coordinates in the model, there will be two

equations of motion. The derivation of the equations of motion are shown in Appendix B, where the Lagrangian in Equation (2.49) is applied to Lagrange's equation (2.31). The equations of motion for the drawwork hoisting system are expressed in Equation (2.52) and (2.53).

$$\left(J_{tot} + m_t\gamma^2\right)\ddot{\theta}_m + \gamma m_t\ddot{z}_c + \gamma m_t g = \tau_m - \tau_{hl} + \tau_{f,m} \tag{2.52}$$

$$\gamma m_t\ddot{\theta}_m + (m_t + m_c)\ddot{z}_c - k_c(z_{wt} - z_c) + (m_t + m_c)g = b_c(\dot{z}_{wt} - \dot{z}_c) - F_{hl} \tag{2.53}$$

The Equations (2.52) and (2.53) governs the dynamics of the hoisting system together with Equations (2.5) and (2.8) which encapsulates the dynamics of the electric motor. These four equations can be merged to one equation by Laplace transforming the equations, and reducing the number of explicit states in the model. A derivation of this final equation is given in Appendix C, which describes the behaviour of the hoisting system for the given system inputs. The system inputs are the motor voltage u, and the position of the water table z_{wt}, which will be influenced by the heave motion induced by ocean waves.

$$\left[\left(J_{tot} + m_t\gamma^2\left(1 - \frac{m_t}{m_t + m_c}\right)\right)s^2 + \left(\frac{K_v K_t}{L_a s + R_a} + B_a\right)s\right]\theta_m = \frac{K_t}{L_a s + R_a}u - \left(1 - \frac{m_t}{m_t + m_c}\right)\tau_{hl} + \tau_{f,m} - \frac{m_t\gamma}{m_t + m_c}(k_c + b_c s)(z_{wt} - z_c) \tag{2.54}$$

In the derivations of the equations of motion, a number of assumptions and simplifications have been made. The reader will find a list below which summarizes these assumptions.

- The drilling line in the block and tackle system is assumed to be massless and have no elastic properties.

- The gears between the motor and the wire drum are assumed to be massless and frictionless.
- The friction exerted on the sheaves from the bearings are assumed to have no static component.
- The calculation of the sheave friction assumes there is no translational acceleration of the respective block.
- The hook load force is assumed to be evenly distributed on all the working lines in the block and tackle system.
- The translational movement of the crown block relative to the water table does not affect the rotational velocity of the sheaves.

Chapter 3

Drill string and well

In this chapter, a model of the dynamics in the drill string, and the drilling mud in the well will be presented. The derivations in this chapter are motivated by the work of Strecker et al. [6]. Therefore, the presentation of the model in this chapter will be brief. Most of the theory formulations in this chapter are based on the author's specialization project [12].

3.1 Drill string

The drawwork hoisting system described in the previous chapter is used to manage the movement of the drill string. As previously discussed, the travelling block is holding the weight of the drill string, and is maneuvering the drill string by utilizing the block and tackle principle. The drill string is used to transfer rotational motion from the top drive down to the drill bit in order to drill through the rock layers below the sea bed. In addition, the drill string is used to transfer drilling mud down hole. This drilling mud is used to cool the drill bit, to transport drilling debris to the surface, and to control the down hole pressure.

The drill string is composed by the bottom hole assembly (BHA), the transition pipe, and the drill pipe. The BHA is composed by a drill bit which is used to break up rock formation below the sea bed, drill collars which are used to apply weight to the drill bit, and drilling stabilizers to keep the assembly centered in the hole. The transition pipe is the pipe segment between the BHA and the drill pipe. The drill pipe consists of multiple 30 meters long stands that are attached to one another at the rig as the drill string is lowered into the well hole.

Drill string model

Inspired by the work of Greenfield et al. [13], the dynamics of the drill string was modelled as a one dimensional elastic rod based on the 1D continuity equation, given as

$$\frac{\partial \sigma_d}{\partial t} = E \frac{\partial v_d}{\partial z}. \tag{3.1}$$

Here, σ_d, E and v_d is the mechanical stress in the drill string, Young's modulus, and the heave velocity of the drill string, respectively. As derived by Dahlen [14], the momentum balance for the drill string yields a relationship between the drill string acceleration $\frac{\partial v_d}{\partial t}$, and the pressure gradient in the drill string $\frac{\partial p_d}{\partial z}$.

$$\rho_d \frac{\partial v_d}{\partial t} = -\frac{\partial p_d}{\partial z} - k_p v_d \tag{3.2}$$

Here, the term $k_p v_d$ accounts for both the force per unit length exerted on the drill string as it slides along the walls of the well, and the viscous drag induced by the movement.

The mud that flows through the drill string leaves the pipe through the drill bit at the end of the drill string. The flow through the drill bit can be modelled as a non-return valve equation, where turbulent flow is assumed. The

flow as a function of the pressure difference over the valve, Δp, is stated as in Egeland et al. [11].

$$q_{bit}(\Delta p) = \begin{cases} C_d A_{\text{TFA}} \sqrt{\frac{2}{\rho_d} \Delta p}, & \text{if } p_i^{bit} > p_{bb}^{bit} \\ 0, & \text{if } p_i^{bit} \leq p_{bb}^{bit} \end{cases} \tag{3.3}$$

Here, C_d is the discharge coefficient of the valve, and A_{TFA} is the total flow area through the bit nozzles. The drilling mud that flows out of the drill string continues up the annulus inside the well, which will be discussed next.

3.2 Well

The well is composed by several subsystems, as indicated in Figure 3.1. The governing equations that will be discussed in this section describes the fluid dynamics of the drilling mud in these subsystems. The choke valve and back pressure pump are located at the top of the sealed annulus, which may be utilized for flow and pressure control in the well. As recommended by the American Petroleum Institute [15], the Herschel-Bulkley rheological model [16] was used for the drilling mud. The model relates the shear rate $\dot{\gamma}$ to the shear stress τ by

$$\tau(\dot{\gamma}) = \left(K_{hb} |\dot{\gamma}|^{n_{hb}-1} + \frac{\tau_0}{|\dot{\gamma}|} \right) \dot{\gamma}, \tag{3.4}$$

where τ_0, K_{hb}, and n_{hb} are the yield point, consistency index and flow index of the fluid, respectively.

To model the fluid dynamics in the well, Mitchell [17] suggests using the 1D continuity equation, which is expressed in equations (3.5) - (3.8). The flow inside the drill string and annulus is assumed to flow in the axial di-

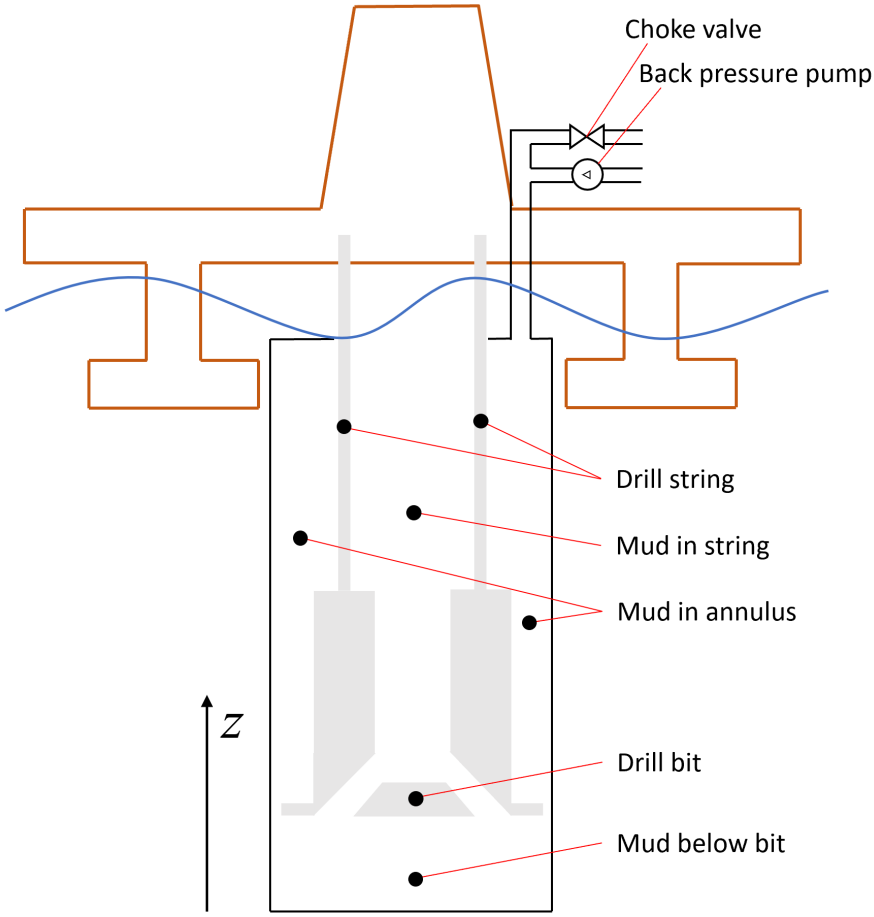

Figure 3.1: Well schematic showing the different subsystems in the well.

rection. The term $\frac{\beta}{A}\frac{\partial q}{\partial z}$ represents advective transport in the mass balance equations (3.5) and (3.7). The latter term in the mass balance, $\left(\frac{\beta}{A}\frac{\partial A}{\partial p}\right)\frac{\partial p}{\partial t}$, encapsulates the effect of compression of the annulus due to the pressure differential from the drill string. Further, Equation (3.6) and (3.8) represents the momentum balances. The forces present in the equations are due to the pressure gradient, friction and gravity, respectively.

$$\frac{\partial p_a}{\partial t} = -\frac{\beta_a}{A_a}\frac{\partial q_a}{\partial z} - \left(\frac{\beta_a}{A_a}\frac{\partial A_a}{\partial p_i}\right)\frac{\partial p_i}{\partial t} \tag{3.5}$$

$$\frac{\partial q_a}{\partial t} = -\frac{A_a}{\rho_a}\frac{\partial p_a}{\partial z} - \frac{1}{\rho_a}[F_{a,in}(q_a, v_i) + F_{a,out}(q_a, v_i)] - A_a g\cos(\theta_d) \tag{3.6}$$

$$\frac{\partial p_i}{\partial t} = -\frac{\beta_i}{A_i}\frac{\partial q_i}{\partial z} - \left(\frac{\beta_i}{A_i}\frac{\partial A_i}{\partial p_a}\right)\frac{\partial p_a}{\partial t} \tag{3.7}$$

$$\frac{\partial q_i}{\partial t} = -\frac{A_i}{\rho_i}\frac{\partial p_i}{\partial z} - \frac{1}{\rho_i}F_i(q_i, v_i) - A_i g\cos(\theta_d) \tag{3.8}$$

The implementation of the model is done by distributing the hyperbolic partial differential equations over a uniform grid spanning the well and the drill string. The main assumptions that were made in the derivations of the well model are listed below.

- Constant parameters was assumed along each subsystem of the distributed model.
- Constant density was assumed inside the drill string and the annulus.
- BHA was assumed to be a rigid body .
- Thermal effects on dynamics were neglected.
- Mud loss to the formation in the well was neglected.
- Hook-strain effect on the drill string was neglected.

Chapter 4

Simulator configuration and model validation

In this chapter, a series of simulations will be discussed to validate the credibility of the models for simulations in later chapters. The models discussed in chapters 2 and 3 were implemented in Matlab, and simulations of the individual models as well as the coupled models will be discussed. First, a simulation of the hoisting system with a specific setup will be addressed. Secondly, a simulation of the drill string and well model will be compared to a data set that has been generated at a drilling rig in the north sea. The source of the data that will be used for validation will remain anonymous, but permission has been granted to publish the figures in this chapter. Lastly, the two models were coupled and simulated as one complete system.

4.1 Hoisting system model validation

In this section, a simulation of the hoisting system model that was derived in chapter 2 will be discussed. The simulation that was performed had the following inputs.

- The hook load was set to a constant value of 2 tons.
- The drawwork motor voltage was set to a constant value of 600 volts.
- The heave motion of the rig was set to follow a sinusoidal movement with an amplitude of 5 meters, and a period of 10 seconds.

Further, the parameters in the hoisting system model were set according to drawwork data sheets produced by National Oilwell Varco [8], and are shown in Table 4.1. The results of the simulation are displayed in Figure 4.1. As shown in the Figure 4.1a, the crown block started out at the same position as the water table. Due to the applied hook load and the mass of the blocks, the CMC translated the crown block a few meters, before converging at an equilibrium. One may also notice that the travelling block was gradually elevated towards the water table, emulating the tripping of a drill string. The effect of the CMC can also be seen in the Figure 4.1b, where the crown block was lagging the water table by approximately one second. In Figure 4.1c, one may observe that the motor power peaked at approximately 5 mega watts in the start of the simulation. Initially, the hoisting system was at rest, so the system needed a significant amount of power to accelerate. Lastly, in Figure 4.1d, the drill line is shown as it was spooled onto the drum. About 8 seconds into the simulation, drill line layer number two was complete, and the remaining drill line was spooled onto layer number three.

R_a	$0.056\ \Omega$	Armature winding resistance
L_a	5 mH	Armature winding inductance
K_v	3.715 Nm/A	Motor constant
K_t	3.715 V/Rad	Motor constant
J_m	$3.35 \cdot 10^{-6}$ kgm^2	Rotor moment of inertia
B_a	26.53 kgm^2/s	Rotational damping coefficient
n_g	$1 : 10.5$	Gear ratio
n_l	12	Working lines in block & tackle setup
k_c	3500 N/m	Spring coefficient in CMC
b_c	5000 Ns/m	Damper coefficient in CMC
μ_s	0.001	Friction coefficient in sheave bearings
$r_{s,i}$	0.1 m	Inner radius in sheaves
r_s	1.524 m	Outer radius in sheaves
r_{dl}	0.022 m	Radius of drill line
λ_{dl}	8.44 kg/m	Mass per unit length of drill line
m_c	1000 kg	Mass of crown block
m_t	1000 kg	Mass of travelling block
m_s	30 kg	Mass of sheave
l_d	2.082 m	Width of wire drum
r_{d0}	0.8 m	Radius of empty drum
J_{d0}	7950 kgm^2	Moment of inertia of empty drum

Table 4.1: Hoisting system parameter table.

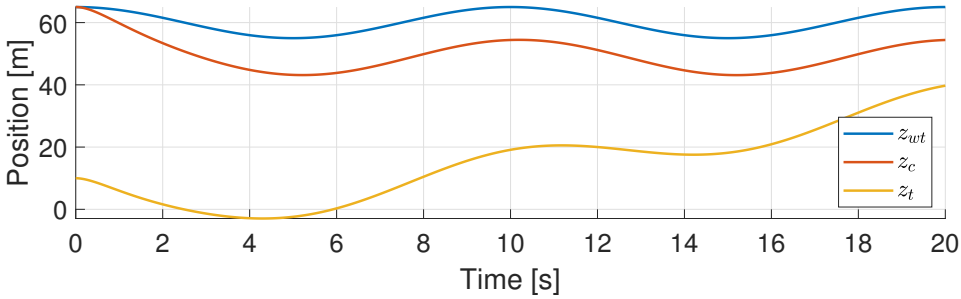

(a) Position of the blocks and the water table.

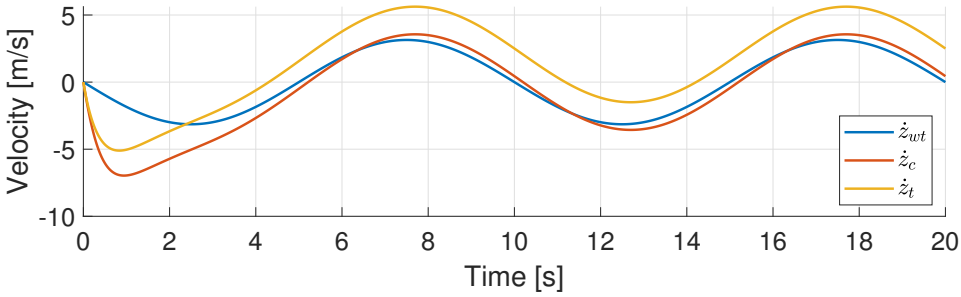

(b) Velocity of the blocks and the water table.

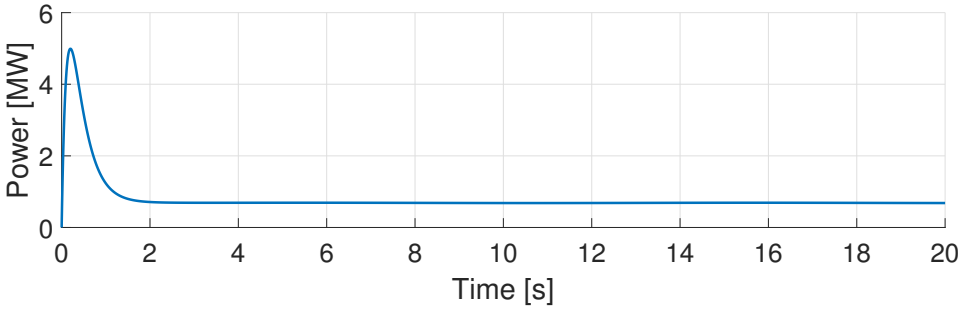

(c) Motor power consumption.

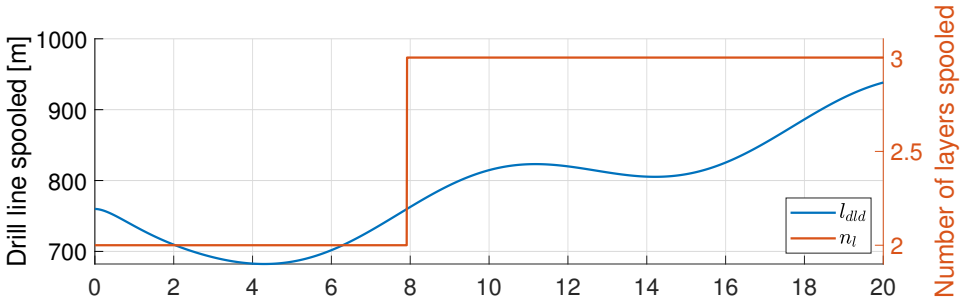

(d) Wire drum status.

Figure 4.1: Simulation of the drawwork hoisting system for model validation.

4.2 Drill string and well model validation

4.2.1 Validation set

The data set that was used for validation of the simulator, hereafter referred to as the validation set, was recorded during a drilling operation in the north sea. The data was recorded for several hours, but only a short time series of the data set will be discussed. The vertical depth of the well was approximately 1600 meters, with a horizontal section approximately 3600 meters long. The total length and the vertical depth of the well are called *the measured depth* and *the total vertical depth*, respectively. The fact that the well curves horizontally caused an increase of the total friction that was exerted on the drill string during the tripping operation. An increase of friction will indeed increase the hook load, which must be taken into consideration upon comparison.

Consider the well profile displayed in Figure 4.2. The time series of the validation set that will be used for comparisons purposes, was extracted at the point in time when the drill string had the position indicated by the red curve. This particular time series was chosen because it matches the conditions which the simulator was implemented for the best. Here, the drill bit has been tripped out approximately 1200 meters from the well bottom, such that the horizontal component of the drill string is minimized, and the well bottom is not influencing the fluid flow and annular pressure down hole. The time series of the validation set contains down hole pressure, mud flow data, as well as hook load measurements that were recorded during a tripping of one stand. The tripping direction was out of the well. The topside mud pump was shut off, and the flow rate through the choke and back pressure pump was zero.

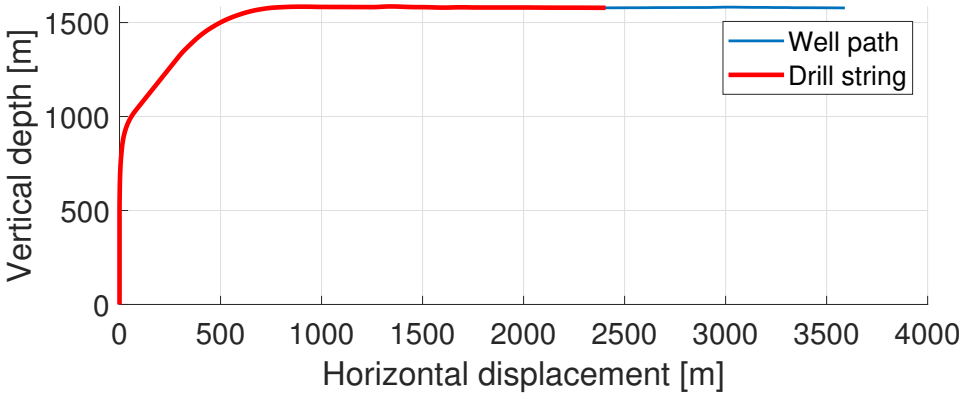

Figure 4.2: Profile of the well in the validation set, red curve represents the location of the drill string.

4.2.2 Drill string and well simulation

The simulator was set to match the boundary conditions present in the validation set. However, the simulator was not implemented for wells with horizontal sections, so the measured depth in the simulator was set to match the total vertical depth that was recorded, approximately 1580 meters. Further, the pressure at the top of the annulus was set to atmospheric pressure. By studying the measured depth in the validation set, displayed in Figure 4.3a, the tripping velocity was set to 1 meter per second with a velocity profile displayed in Figure 4.3b. The parameters that were used in the simulator are shown in Table 4.2.

With the simulator configured accordingly, the resulting hook load and down hole pressure can be viewed in Figure 4.3c. Notice that the measured hook load from the validation set starts off at 0 tons, which indicates that the drill string was in slips before - and after the tripping. The maximum hook load that was measured in the validation set was about 90 tons, whereas the simulated hook load had a maximum about 50 tons. The main reason for this discrepancy is the horizontal section causing an increase of the total friction force exerted on the drill string. In Figure 4.3d, the down

hole pressure relative to the static pressure is displayed. Since this is a tripping out of the well, a decompression occurs which causes the down hole pressure to drop. By comparing the simulated pressure and the measured pressure from the validation set, one may observe that the pressure drop is more significant in the validation set. The reason for this can only be speculated in, but it seems that the simulated mud does not need as much delta pressure to start flowing. Another reason might be the increased friction exerted on the drill string, which may cause the tripping movement down hole to be uneven. Strecker et al. [5] explains a similar phenomena as a jump of the drill bit. As the top of the drill string starts to move, the tension in the drill string must overcome the friction and drag forces before the bit starts to move. When sufficient tension is present, the bit jumps with a velocity greater than the tripping velocity. This jump induces a transient pressure drop. The pressure drop displayed in the figure may be caused by this this phenomena. However, even though there are some differences between the simulator and the validation set, the plots show a likeness between the model and the real world. This simulation data was also evaluated by Equinor.

L_d	1600 m	Length of drill string
L_{BHA}	100 m	Length of BHA
L_{bb}	40 m	Distance from drill bit to bottom of well
A_d	$9.4 \cdot 10^{-3}$ m^2	Cross sectional area of drill string
A_w	$3.66 \cdot 10^{-2}$ m^2	Cross sectional area of well
A_{TFA}	$9.4 \cdot 10^{-3}$ m^2	Total flow area through bit nozzles
C_d	0.98	Valve flow coefficient
μ_w	0.2	Kinematic friction coefficient in well
θ_d	0 rad	Inclination angle in well
g	9.81 m/s^2	Acceleration of gravity
λ_d	30 kg/m	Mass per unit length of drill string
m_{BHA}	12000 kg	Mass of BHA
ρ_d	1060 kg/m^3	Density of mud in drill string
ρ_a	1060 kg/m^3	Density of mud in annulus
ρ_{bb}	1060 kg/m^3	Density of mud below bit
ρ_p	7800 kg/m^3	Density of drill string (pipe)
β_d	1.8 GPa	Effective bulk modulus of mud in drill string
β_a	1.6 GPa	Effective bulk modulus of mud in annulus
β_{bb}	1.8 GPa	Effective bulk modulus of mud below bit
E	206.8 GPa	Drill string Young's modulus
τ_0	5 Pa	Yield point in Herschel-Bulkley model
K_{hb}	0.2 Pa s	Consistency index
n_{hb}	0.7	Flow index

Table 4.2: Drill string and well parameter table.

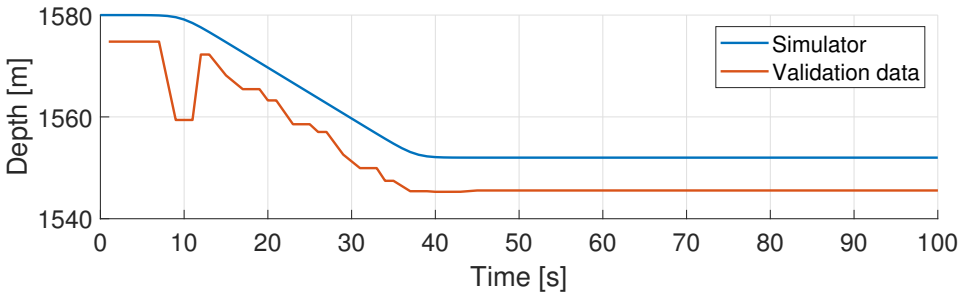

(a) Total vertical depth

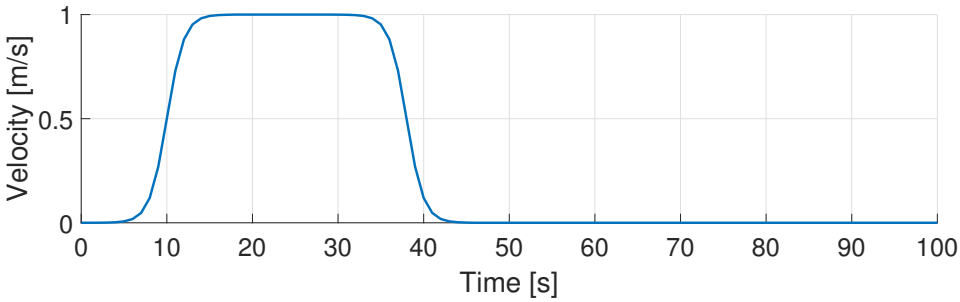

(b) Tripping velocity.

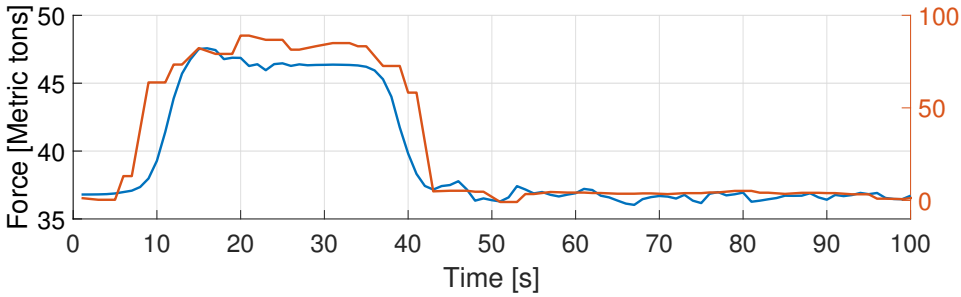

(c) hook load.

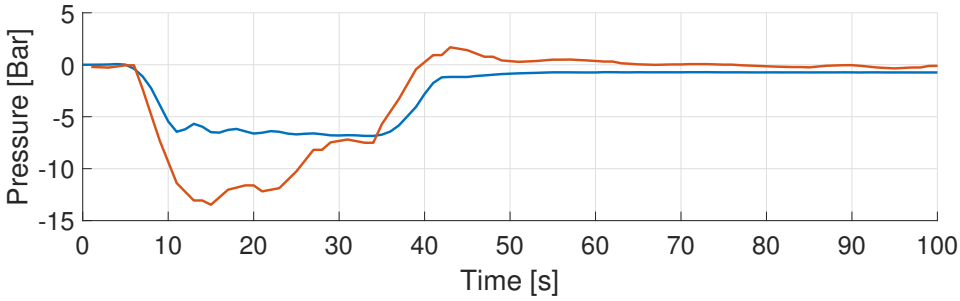

(d) Relative pressure down hole

Figure 4.3: Simulation data of the drill string and well model in blue together with the validation data in red. The relative pressure plot is displaying the dynamic pressure relative to the static pressure down hole.

4.3 Complete simulator validation

In this section, a simulation of the hoisting system model coupled with the string and well model will be discussed. The two models are coupled by the drill string velocity, and the hook load, as shown in the block diagram in Figure 4.4.

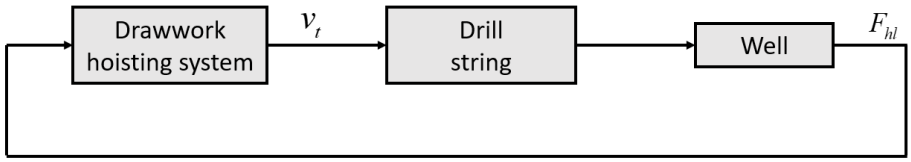

Figure 4.4: Block diagram of the hoisting system model coupled with the drill string and well model.

The configuration of the models are similar to the previous sections, with an adjustment of the CMC settings, b_c and k_c. The final values of $b_c = 10^7$ Ns/m, and $k_c = 3500$ N/m was chosen to achieve stable simulations. The coupled models were simulated with the following inputs, similarly to the simulation of the hoisting system in section 4.1.

- The drawwork motor voltage was set to a constant value of 600 volts.
- The heave motion was set to follow a sinusoidal movement with 5 meters amplitude a period of 10 seconds.

The results of this simulation can be viewed in Figure 4.5. As displayed in Figure 4.5a, the travelling block was elevated about 40 meters in the 20 seconds simulation time. This represents a tripping velocity that is greater than what is normal in the north sea. This demonstrates that the hoisting system has the necessary capacity, consuming an average power of about 2,3 mega watts. This is equivalent to 67% of the drawwork motors limit. Further, in Figure 4.5b, one may observe that the deviation between the

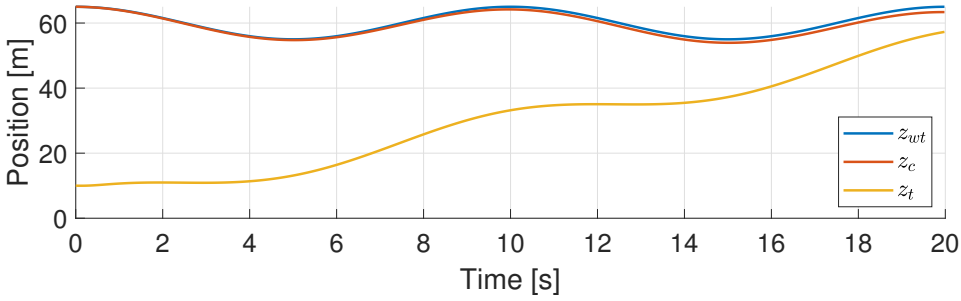

(a) Block positions.

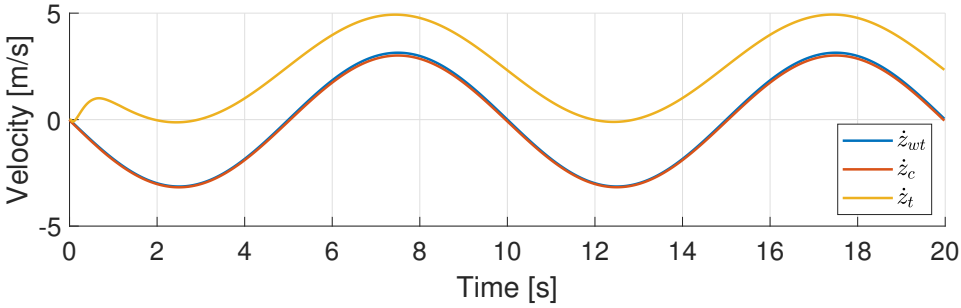

(b) Block velocities.

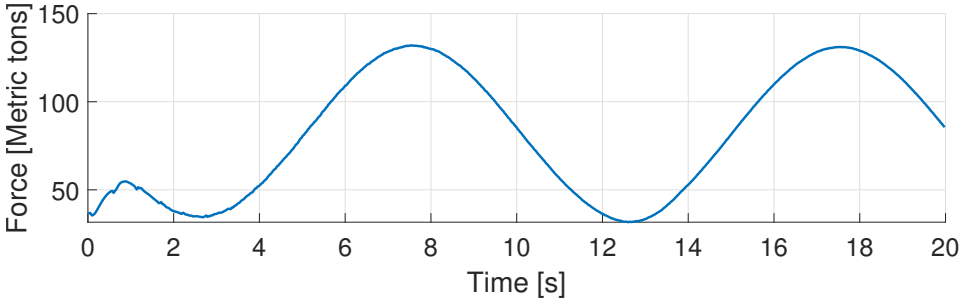

(c) hook load.

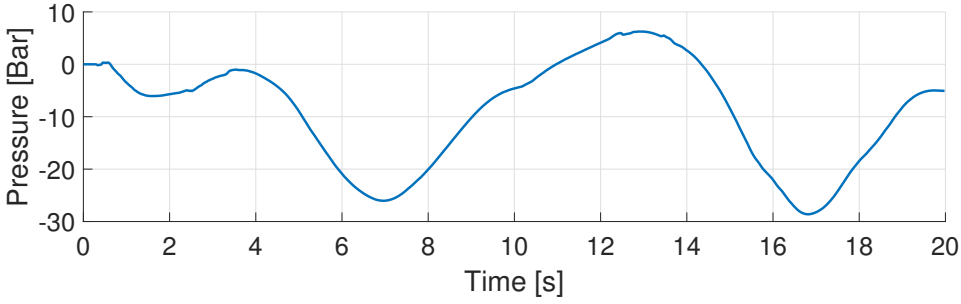

(d) Relative pressure down hole.

Figure 4.5: Simulation of the hoisting system model coupled with the drill string and well model for a complete model validation.

crown block- and water table velocity was negligible. This indicates that for this setup, the waves are barely getting damped through the passive compensator. In order to accomplish a better damping of the heave motion, simulations were done with decreasing spring- and damping terms in the CMC, without any major improvements. Furthermore, the pressure oscillations down hole, shown in Figure 4.5d, was barely impacted by the CMC adjustments. A talk with Equinor confirmed that the CMC is commonly used during drilling operations, where the drill bit is at the bottom of the well. However, during tripping, the drill bit is elevated from the ground, rendering the CMC inefficient for heave compensation. This motivates an active hoisting system that isolates the drill string motion from the heave motion during tripping. A control strategy for this will be further discussed in the next chapter.

Chapter 5

Motion control

In this chapter, a heave compensation controller for tripping will be proposed. The drawwork model that was presented in chapter 2 will be used as a frame work for the derivation. First, a linearization and simplification of the drawwork model will be justified. Next, a pole-placement algorithm will be used to derive a controller that is able to suppress disturbances, isolate the drill string from the wave-induced heave motion and control the tripping velocity. Other optimal control strategies like Linear Quadratic Regulator (LQR) were considered over the course of this work, but the pole-placement controller was chosen because of its satisfactory performance and its intuitive derivation. Furthermore, in the author's specialization project [12], the simplest controller with disturbance feed forward was considered to be the most effective strategy for heave compensated tripping.

5.1 Model simplification

The equation of motion that was derived in chapter 2 is expressed in Equation (2.54), and is restated here.

$$\left[\left(J_{tot} + m_t\gamma^2\left(1 - \frac{m_t}{m_t + m_c}\right)\right)s^2 + \left(\frac{K_v K_t}{L_a s + R_a} + B_a\right)s\right]\theta_m = \frac{K_t}{L_a s + R_a}u - f_{hl}(\tau_{hl}) + \tau_{f,m}(\omega_m) - f_c(z_{wt}, z_c) \tag{5.1}$$

where the functions f_{hl} and f_c are expressed as

$$f_{hl}(\tau_{hl}) = \left(1 - \frac{m_t}{m_t + m_c}\right)\tau_{hl}, \tag{5.2}$$

$$f_c(z_{wt}, z_c) = \frac{m_t\gamma}{m_t + m_c}(k_c + b_c s)(z_{wt} - z_c). \tag{5.3}$$

One may claim that the nonlinear friction torque $\tau_{f,m}(\omega_m)$, defined in Equation (2.27), can be neglected in the model that is used for control system design. In order to validate this claim, consider Figure 5.1. In Figure 5.1a, the friction torque has been plotted for increasing values of the motor rotational velocity, ω_m, where the system parameters in Table 4.1 has been used. One may observe that the maximum friction torque that may occur in the system is approximately 5.4 Newton meters. For comparison, in Figure 5.1b, the motor torque has been plotted for a scenario with constant tripping velocity of 0.1 meter per second, and a constant hook load of 10 tons. Clearly, the friction torque exerted on the hoisting system is negligible upon comparison with the torque that is necessary to accelerate the load to a constant velocity. By this argument, the model is reduced by neglecting the nonlinear friction term in the control system design.

Further, the influence of the crown mounted compensator will be neglected

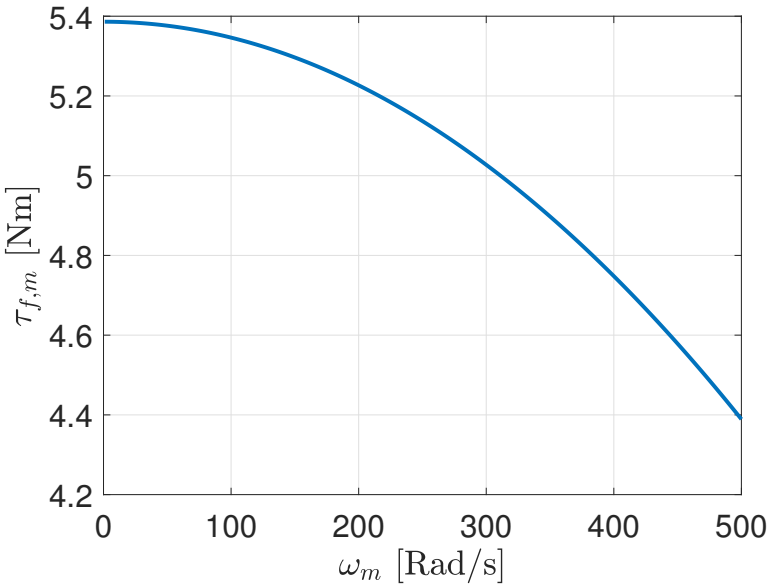

(a) Friction curve, defined in Equation (2.27).

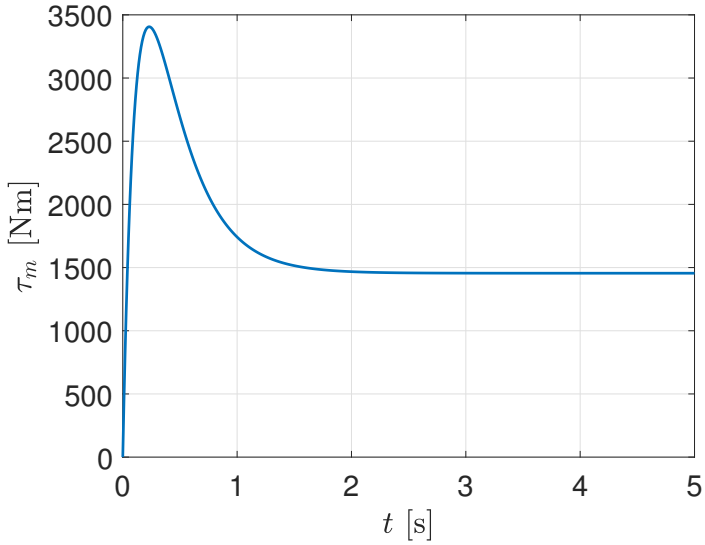

(b) Motor torque curve, tripping speed was set to $v_t = 0.1$ m/s and hook load constant at $F_{hl} = 100$ kN.

Figure 5.1: Friction curve and motor torque curve generated with data from Table 4.1.

in the model used for control system design. As discussed in chapter 4, the CMC does not work effectively when the drill bit is not in contact with the bottom of the well. For this reason, the CMC should be locked during tripping, and will therefore not be considered as part of the system model in the derivations of the control strategy. In order to simplify the equations of motion to not take the CMC movement into consideration, the position of the water table is set equal to the position of the crown block, i.e. $z_{wt} = z_c$.

With these simplifications, the resulting model that will be used for the derivation of the control strategy is expressed as follows.

$$\left[\left(J_{tot} + m_t\gamma^2\left(1 - \frac{m_t}{m_t + m_c}\right)\right)s^2 + \left(\frac{K_v K_t}{L_a s + R_a} + B_a\right)s\right]\theta_m = \frac{K_t}{L_a s + R_a}u - \left(1 - \frac{m_t}{m_t + m_c}\right)\tau_{hl} \tag{5.4}$$

5.2 Control system design

In this section, the heave compensation control algorithm will be derived which will be used in simulations with active hoisting. This analysis is motivated by a pole-placement algorithm that is described by Fossen [18], which derives a feedback control algorithm for a 2nd order system. The derivation is done in the time domain, where the error dynamics of the closed loop system is exploited. By formulating this error dynamics as a standard 2nd order system, the relative damping factor, and the control bandwidth may be chosen explicitly. For the sake of similarity, the equation of motion will be transformed into the time domain. First, some notation

will be introduced to make the derivation easier to follow.

$$\begin{aligned} \alpha &= J_{tot} + m_t\gamma^2\left(1 - \frac{m_t}{m_t + m_c}\right) \\ \beta &= 1 - \frac{m_t}{m_t + m_c} \end{aligned} \tag{5.5}$$

Applying this notation to Equation (5.4), and multiplying both sides by the term $L_a s + R_a$ yields

$$\begin{aligned} \left[L_a\alpha s^2 + (R_a\alpha + L_aB_a)s + K_vK_t + R_aB_a\right]\theta_m s = \\ K_t u - (L_a\beta s + R_a\beta)\tau_{hl}. \end{aligned} \tag{5.6}$$

Laplace inverting this equation into the time domain yields a 2nd order equation,

$$\begin{aligned} L_a\alpha\ddot{\omega}_m + (R_a\alpha + L_aB_a)\dot{\omega}_m + (K_vK_t + R_aB_a)\omega_m = \\ K_t u - L_a\beta\dot{\tau}_{hl} - R_a\beta\tau_{hl}, \end{aligned} \tag{5.7}$$

where the relationship $\theta_m s = \omega_m$ has been used as the state of the model.

Recall that the objective of this controller is to regulate the motion of the drill string. The drill string velocity is set by the velocity of the travelling block. When assuming that the CMC is locked, the tripping velocity can be observed by measuring the heave motion of the rig, and the rotational velocity of the motor. In order to express the model in terms of the tripping velocity, consider the following change of variable.

$$v_t = \gamma\omega_m + v_{rig} \Longleftrightarrow \omega_m = \frac{v_t - v_{rig}}{\gamma} \tag{5.8}$$

This change of variable and some algebraic manipulation yields the follow-

ing model

$$\frac{L_a\alpha}{\gamma K_t}\ddot{v}_t + \frac{R_a\alpha + L_aB_a}{\gamma K_t}\dot{v}_t + \frac{K_vK_t + R_aB_a}{\gamma K_t}v_t = u - \frac{L_a\beta}{K_t}\dot{\tau}_{hl} - \frac{R_a\beta}{K_t}\tau_{hl} + \frac{L_a\alpha}{\gamma K_t}\ddot{v}_{rig} + \frac{R_a\alpha + L_aB_a}{\gamma K_t}\dot{v}_{rig} + \frac{K_vK_t + R_aB_a}{\gamma K_t}v_{rig}, \tag{5.9}$$

where the tripping velocity, v_t, is considered the state of the model, and the motor voltage u, the hook load torque τ_{hl}, and the heave velocity of the rig, v_{rig}, are considered the system inputs. Since the motor voltage is the only input that can be adjusted by the controller, it will be denoted the control input in the system. The other inputs acts as disturbances in the system. The influence of the disturbance inputs may be minimized by measuring their states, and cancelling them out in a feed forward loop. Clearly, such a control strategy requires an estimate of these inputs. The details on the acquisition of these inputs is described in chapter 6. Consider the control input u to be composed by a feedback input as well as a feed forward input, expressed as

$$u = u_{fb} + u_{ff}. \tag{5.10}$$

Observe that a feed forward input expressed as

$$u_{ff} = \frac{L_a\beta}{K_t}\dot{\tau}_{hl} + \frac{R_a\beta}{K_t}\tau_{hl} - \frac{L_a\alpha}{\gamma K_t}\ddot{v}_{rig} - \frac{R_a\alpha + L_aB_a}{\gamma K_t}\dot{v}_{rig} - \frac{K_vK_t + R_aB_a}{\gamma K_t}v_{rig} \tag{5.11}$$

will reduce Equation (5.9) to the following, by inserting the composed control input in Equation (5.10).

$$\frac{L_a\alpha}{\gamma K_t}\ddot{v}_t + \frac{R_a\alpha + L_aB_a}{\gamma K_t}\dot{v}_t + \frac{K_vK_t + R_aB_a}{\gamma K_t}v_t = u_{fb} \tag{5.12}$$

Assuming that the tripping velocity is observable through measurements or state estimators, a feedback control law can be constructed which will

regulate the tripping velocity to a reference velocity, v_r.

Motivated by the pole-placement algorithm described by Fossen [18], the error dynamics of the model can be controlled by a feedback controller composed by a PD feedback law as well as a reference feed forward law. Consider the feedback input, u_{fb}, composed by the following.

$$\begin{aligned} u_{fb} = &\underbrace{-K_p(v_r - v_t) - K_d(\dot{v}_r - \dot{v}_t)}_{\text{PD feedback}} \\ &\underbrace{+ \frac{L_a\alpha}{\gamma K_t}\ddot{v}_r + \frac{R_a\alpha + L_aB_a}{\gamma K_t}\dot{v}_r + \frac{K_vK_t + R_aB_a}{\gamma K_t}v_r}_{\text{Reference feed forward}} \end{aligned} \tag{5.13}$$

By inserting this feedback input into Equation (5.12), the dynamics of the tripping velocity error, $\tilde{v}_t = v_r - v_t$, can be described as follows.

$$\frac{L_a\alpha}{\gamma K_t}\dddot{\tilde{v}}_t + \left(\frac{R_a\alpha + L_aB_a}{\gamma K_t} + K_d\right)\ddot{\tilde{v}}_t + \left(\frac{K_vK_t + R_aB_a}{\gamma K_t} + K_p\right)\dot{\tilde{v}}_t + \tilde{v}_t = 0. \tag{5.14}$$

Observe that the error dynamics described in this equation is on the standard form of a 2nd order differential equation, stated as

$$\ddot{x} + 2\zeta\omega_n\dot{x} + \omega_n^2 x = 0, \tag{5.15}$$

for a given state x. By matching the terms, the relative damping factor, ζ, and the natural frequency, ω_n, of the error model can be expressed by the following relationship.

$$\begin{aligned} 2\zeta\omega_n &= \frac{R_a\alpha + L_aB_a}{L_a\alpha} + \frac{\gamma K_t}{L_a\alpha}K_d \\ \omega_n^2 &= \frac{K_vK_t + R_aB_a}{L_a\alpha} + \frac{\gamma K_t}{L_a\alpha}K_p \end{aligned} \tag{5.16}$$

The natural frequency ω_n can be related to the system bandwidth by the following definition, given in Fossen [18].

Definition 5.1. Control bandwidth

The control bandwidth of a system $y = h(s)u$ with negative unity feedback is defined as the frequency ω_b at which the loop transfer function $l(s) = h(s) \cdot 1$ is

$$|l(j\omega)|_{\omega=\omega_b} = \frac{\sqrt{2}}{2} \tag{5.17}$$

From this definition, it can be shown that the control bandwidth for a given 2nd order system as described in Equation (5.15) with negative unity feedback is

$$\omega_b = \omega_n \sqrt{1 - 2\zeta^2 + \sqrt{4\zeta^4 - 4\zeta^2 + 2}}. \tag{5.18}$$

By explicitly choosing the relative damping factor, and the control bandwidth of the error dynamics, the controller gains can be calculated by substituting the natural frequency in the equation set (5.16). Solving the equations for the control gains, K_p and K_d, yields the following expressions.

$$K_p = \frac{L_a \alpha \omega_b^2}{\gamma K_t (1 - 2\zeta^2 + \sqrt{4\zeta^4 - 4\zeta^2 + 2})} - \frac{K_v K_t + R_a B_a}{\gamma K_t} \tag{5.19}$$

$$K_d = \frac{2 L_a \alpha \zeta \omega_b}{\gamma K_t \sqrt{1 - 2\zeta^2 + \sqrt{4\zeta^4 - 4\zeta^2 + 2}}} - \frac{R_a \alpha + L_a B_a}{\gamma K_t} \tag{5.20}$$

Because of the model inaccuracies and simplifications previously discussed, the control strategy proposed so far will not be able to suppress the influence of ocean waves perfectly. As a matter of fact, these discrepancies may cause the error dynamics to not converge to zero, resulting in a steady state error. To cope with these uncertainties, the feedback control input can be augmented with an integral term. With this augmentation, any steady state error will be integrated over time, rendering the error dynamics to zero despite of model inaccuracies. Fossen [18] suggests setting the integral gain

K_i, based on the natural frequency of the system, and the proportional gain in the controller, according to

$$K_i = \frac{\omega_n}{10} K_p. \tag{5.21}$$

The proposed control law can be summarized as follows.

$$\begin{aligned} u = & \underbrace{-K_p \tilde{v}_t - K_i \int_0^t \tilde{v}_t(\tau) d\tau - K_d \dot{\tilde{v}}_t}_{\text{PID feedback}} \\ & \underbrace{+\frac{L_a \alpha}{\gamma K_t} \ddot{v}_r + \frac{R_a \alpha + L_a B_a}{\gamma K_t} \dot{v}_r + \frac{K_v K_t + R_a B_a}{\gamma K_t} v_r}_{\text{Reference feed forward}} \\ & \underbrace{+\frac{L_a \beta}{K_t} \dot{\tau}_{hl} + \frac{R_a \beta}{K_t} \tau_{hl} - \frac{L_a \alpha}{\gamma K_t} \ddot{v}_{rig} - \frac{R_a \alpha + L_a B_a}{\gamma K_t} \dot{v}_{rig} - \frac{K_v K_t + R_a B_a}{\gamma K_t} v_{rig}}_{\text{Disturbance feed forward}} \end{aligned} \tag{5.22}$$

The controller may be tuned to a satisfactory response time by setting the relative damping coefficient ζ, and the system bandwidth ω_b.

Further, as previously discussed, this control system can only be realized if all the system inputs in the equation above can be observed and estimated. This will be further discussed in the next chapter.

Chapter 6

System inputs

The control strategy that was derived in the previous chapter can only be realized if the necessary inputs are available through measurement or estimation. The performance of the controller is highly related to the accuracy and precision of these estimates. In this chapter, the acquisition of the necessary system inputs will be discussed. In addition, based on theory from the author's specialization project [12], a wave model that was used in the simulations will be presented, and a tripping velocity trajectory will be proposed.

6.1 Measurements

6.1.1 Motion reference unit

The motion reference unit (MRU) is used for acceleration measurements as well as attitude measurements on the rig. A motion reference unit contains several instruments, but the most critical instruments are the accelerometer and the angular rate sensor. The MRU is typically located close to the center

of gravity of the rig to simplify computations. Kongsbergs fifth generation MRU [19] was recommended by Equinor, and will be considered in this work. It gives high precision measurements of the three axis accelerations of the rig. The accelerometer in the MRU will be used to estimate the heave motion of the rig. According to Beard et al. [20], the output of an accelerometer can be modelled as

$$\hat{a}_{rig} = k_{rig} a_{rig} + \beta_{rig} + \eta_{rig}, \tag{6.1}$$

where $\hat{a}_{rig}$ is the accelerometer output, k_{rig} is a scaling gain, a_{rig} is the true acceleration, β_{rig} is a bias term, and η_{rig} is a zero mean Gaussian noise term. According to Kongsberg, the noise component is expected to have a standard deviation $\eta_{rig} = 0.01$ m/s^2.

6.1.2 Load cell

The hook load measurement is one of the most important measurements for drilling operations as it is used to estimate the weight on the drill bit. For the purpose of heave compensated tripping however, the hook load measurement must be obtained to fulfill the disturbance feed forward section of the control law in Equation (5.22). Because of the importance of this measurement, it has been subject to research for a long time. Cayeux et al. [7] studied how friction forces in the sheaves may influence the hook load measurement when a load cell is placed on the dead line anchor. The location of the load cell plays a crucial role in the accuracy of the hook load estimate. In Figure 6.1, a schematic of the drawwork hoisting system with the most common load cell locations is displayed. The top drive sensor is located at the connection point between the top drive and the travelling block. This location of the load cell removes the necessity of a precise model of the hoisting system to correct the measurement. On the other hand, it is a more

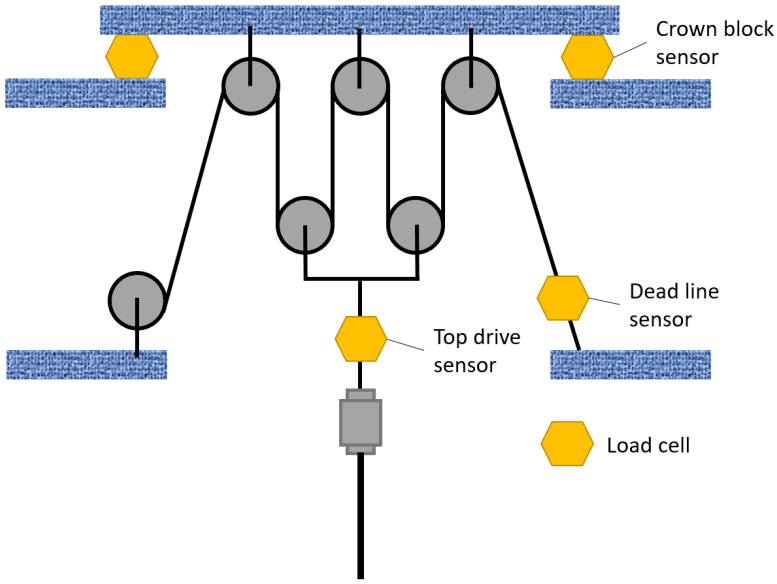

Figure 6.1: Drawwork schematic where common load cell locations for hook load measurements are indicated.

difficult location to access with communication cables. Further, two other common locations for the load cell are at the crown block and at the dead line anchor. Cayeux et al. [21] did experiments on how the hoisting direction influenced the precision of the hook load measurements. The standard deviation of the hook load measurements for upward movement was 300 kg, and 250 kg for downward movement of the travelling block. In addition, by analyzing data from a platform in the North Sea, they discovered that the elasticity of the drill line is the cause of hook load oscillations with an amplitude of 4000 kg with a period in range of one second. A low pass filter was recommended to reduce these oscillations. The data was acquired with a sampling rate of 4 Hz, which will also be used in the simulations in this work.

In order to simplify computations in the simulations, the assumption was made that the load cell is located at the top of the top drive. Under this

assumption, the output of the load cell was modelled as follows.

$$\hat{F}_{hl} = k_{hl} F_{hl} + \eta_{hl} \tag{6.2}$$

Here, $\hat{F}_{hl}$ is the measured hook load from the load cell, k_{hl} is a scaling gain, F_{hl} is the true hook load, and η_{hl} is a zero mean Gaussian noise term. Based on the results of Cayeux et al. [21], the noise term was modelled with a standard deviation $\eta_{hl} = 3$ kN.

6.1.3 Encoder

The angular velocity of the motor must be obtained in order to estimate the tripping velocity of the drill string. This signal may be acquired by mounting an encoder to the rotor of the motor, or to the axle of the wire drum. Similar to the other measurements, the angular velocity of the motor was modelled as follows.

$$\hat{\omega}_m = k_m \omega_m + \eta_m \tag{6.3}$$

Here, $\hat{\omega}_m$ is the measured angular velocity from the encoder, k_m is a scaling gain, ω_m is the true angular velocity of the motor, and η_m is a zero mean Gaussian noise term.

6.2 Heave velocity estimation

It is necessary to estimate the heave velocity of the rig in order to control the velocity of the drill string. As expressed in the control law in Equation (5.22), the heave velocity is essential for both the PID feedback loop, and the disturbance feed forward loop in the controller. The heave velocity is

not observable from the acceleration measurement because of the unknown initial value. Furthermore, as described in the previous section, the acceleration measurement is contaminated with noise. Even if the initial velocity was known, an integration of the noise contaminated acceleration measurement would result in unacceptable drift. To illustrate this, consider Figure 6.2. To simplify the illustration, the rig was assumed to be moving with a sinusoidal motion with a period of 20 seconds. This may be expressed as

$$z_{rig}(t) = \sin(\frac{\pi}{10}t), \tag{6.4}$$

which may be used to calculate the rigs respective heave velocity and acceleration. In the figure, this heave velocity is compared with a pure integration of the heave acceleration, where measurement noise has been added. As one may observe, the discrepancy in the initial value causes an initial error that persists. Furthermore, the integrated heave velocity drifts as time progresses, rendering the estimate useless for the control system. However, the fact that the heave acceleration and velocity originates from wave motion implies a zero mean value. This fact may be exploited in a heave filter where the drift can be eliminated.

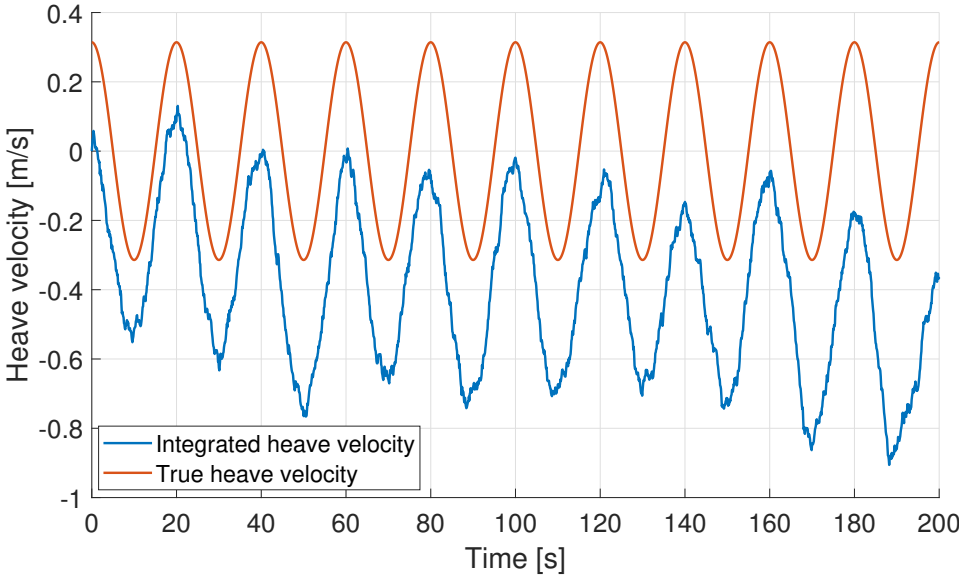

Figure 6.2: Heave velocity calculated from Equation (6.4) together with estimated heave velocity obtained through pure integration of noise contaminated heave acceleration.

6.2.1 Heave filter

The heave filter that was used to estimate the heave motion of the rig was first introduced by Godhavn [22], and has the objective to fulfill the following requirements.

- Integration of the input.
- Eliminating the bias β_{rig} in Equation (6.1).
- Minimize the influence of measurement noise η_{rig}.
- Neglectable filter-induced estimation errors.
- Low settling time.

A straight forward way of filtering out the slow varying bias is to apply a high-pass filter with an integrator to the measured acceleration in Equation

(6.1). The proposed filter has the following form.

$$H_{hf}(s) = \frac{\hat{v}_{rig}}{\hat{a}_{rig}}(s) = \frac{s}{s^2 + 2\zeta\omega_c s + \omega_c^2} \tag{6.5}$$

Here, s is the Laplace variable, ζ is the relative damping coefficient, and ω_c is the cutoff frequency of the filter. The relative damping coefficient was set to $\zeta = \frac{1}{\sqrt{2}}$, to obtain critical damping. Consider Figure 6.3, where the bode plot of the transfer function of the pure integrator and the heave filter with two different cutoff frequencies are displayed. For the filter, the

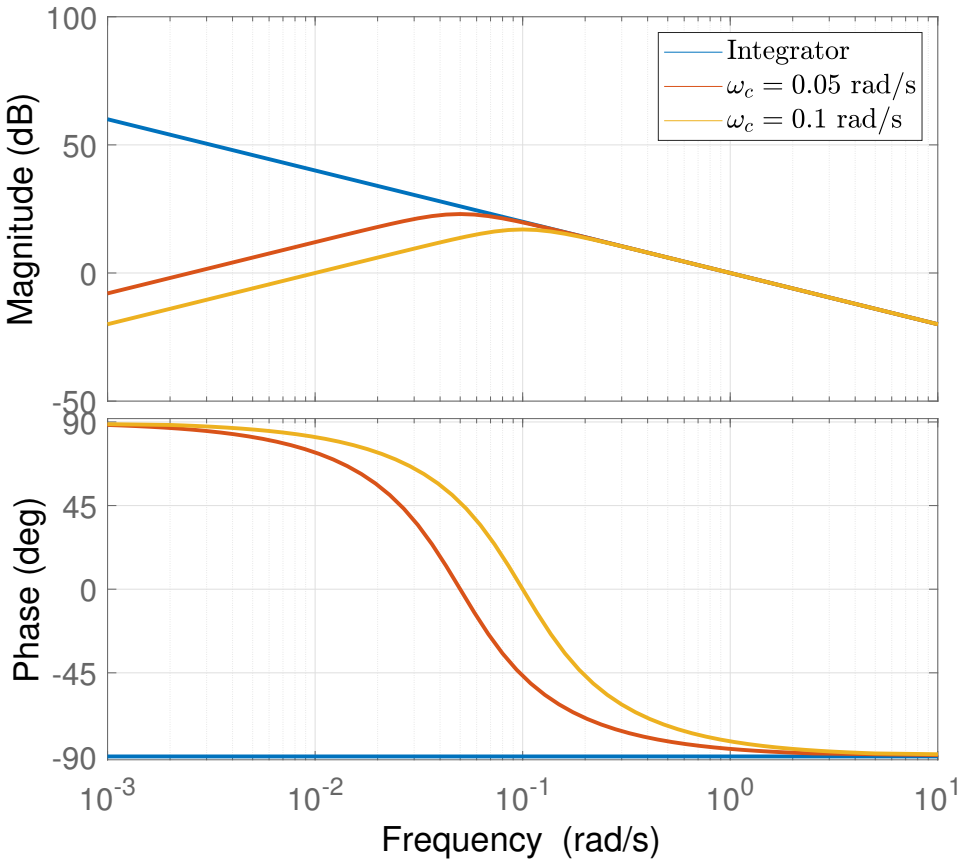

Figure 6.3: Bode plot of the transfer function of a pure integrator and the heave filter with two different cutoff frequencies.

optimal phase for integration of -90^o is not obtained before well after the cutoff frequency. This means that the low frequencies will induce a phase error that will result in major estimation discrepancies. For this reason, it would be beneficial to reduce the cutoff frequency, as indicated by the red curve. However, decreasing the value of the cutoff frequency will increase the settling time of the filter, and reduce the filter's ability to suppress noise. Thus, an optimal cutoff frequency should be obtained by formulating this problem as an optimization problem. As done by Richter et al. [23], an expression of the estimation error may be formulated as a cost function. By solving this optimization problem analytically, an adaptive law for the optimal cutoff frequency can be expressed as

$$\omega_{c,opt} = \frac{1}{2^{3/2}} \left(\frac{2\eta_{rig}^2 \omega_p^2}{A_p^2} \right)^{1/5} . \tag{6.6}$$

Here, η_{rig}^2 is the variance of the heave acceleration measurement noise, ω_p is the dominant frequency of the waves, and A_p is the mean wave height. Godhavn [22] suggests obtaining the dominant frequency by applying a real-time fast Fourier transform to the measured acceleration. Let $a_{rig}^*(j\omega)$ be the Fourier transform of the measured $\hat{a}_{rig}$. Then, the Fourier transform of the heave velocity may be obtained as follows.

$$v_{rig}^*(j\omega) = \frac{1}{j\omega} a_{rig}^*(j\omega) \tag{6.7}$$

Thus, the dominant frequency may be calculated as the argument that maximizes the magnitude of the Fourier transform of the heave velocity.

$$\omega_p = \underset{\omega}{\operatorname{argmax}} \, |v_{rig}^*(j\omega)| \tag{6.8}$$

Further, Richter et al. [23] suggests the mean wave height to be approxi-

mated by using N buffered acceleration measurements.

$$A_p = \sqrt{\frac{2}{N}\sum_{j=0}^{N}\frac{a_j^2}{\omega_p^4}}, \tag{6.9}$$

Here, a_j is the j$^{\text{th}}$ acceleration measurement in $\hat{a}_{rig}$.

By applying this filter to the measured heave acceleration, the estimated heave velocity tracks the true heave velocity without drifting as with pure integration. This is illustrated in Figure 6.4a, and the respective measurement errors can be viewed in Figure 6.4b. As one may observe in the figure, the filtered velocity estimate starts off with incorrect initial value. This is easiest to observe in the error plot in Figure 6.4b. Within the time of one wave period, the error has settled at an average less than 0.1 m/s. The pure integrator on the other hand, starts drifting as previously discussed. This plot shows how the heave filter can be used to eliminating the drift as well as settling within a reasonable time even when the initial condition is unknown.

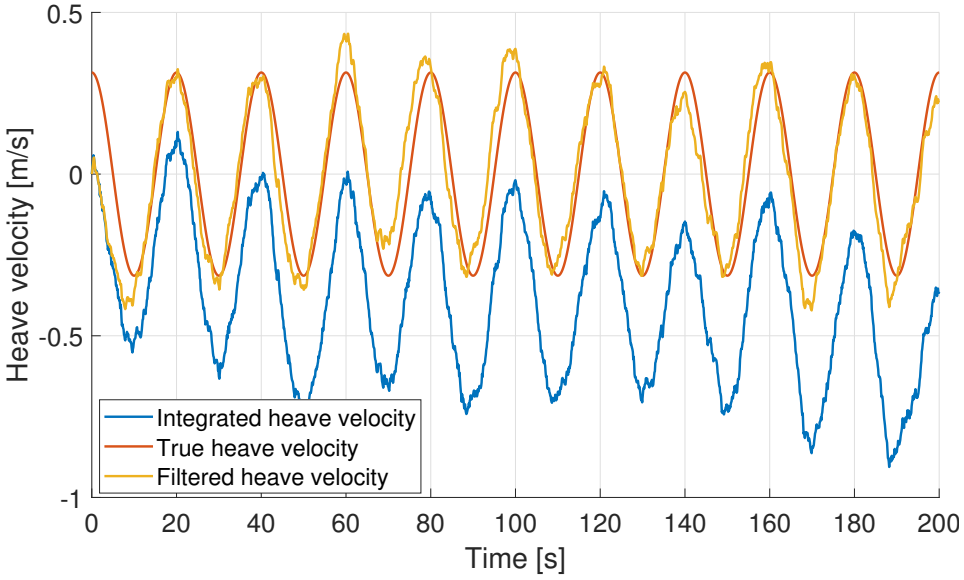

(a) Heave velocities.

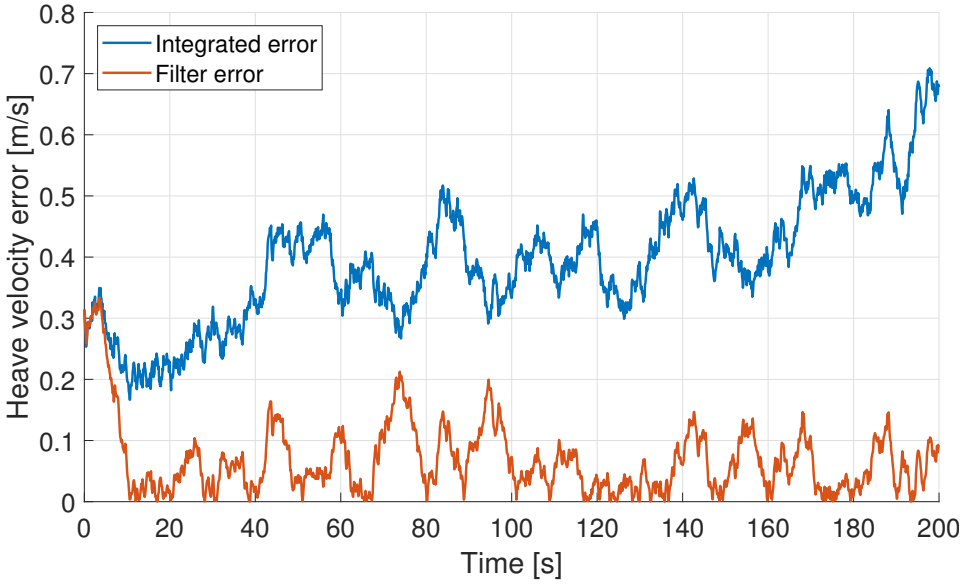

(b) Estimator error plot.

Figure 6.4: Estimated heave velocity generated by the heave filter, and by pure integration compared with the true heave velocity calculated from Equation (6.4). The respective heave velocities are displayed in Figure (a), and the errors of the respective estimates are displayed in Figure (b).

6.3 Wave model

To simulate realistic heave motion, a realistic model of the waves is necessary. Such models are typically characterized by a spectrum of wave frequencies with corresponding wave amplitudes. The doubly peaked Thorsethaugen spectrum [24] was developed specifically for the waves in the North Sea by curve fitting experimental data. The spectrum includes both the effect of newly developed waves (high-frequency waves) and swell (low-frequency waves), and is standardized under the Norsok Standard [25]. The spectrum density function $S(\omega)$ is plotted in Figure 6.5 with a set of peak frequencies. The Norsok Standard defines the significant wave height as four times the standard deviations of the surface elevation. In this figure, the significant wave height was set to $H_s = 6$ m. As one may observe in the figure, if the peak frequency ω_0 is chosen less than approximately 0.6 rad/s, the two peaks merge to one peak, becoming a spectrum where the swell dominates. The amplitude of the waves follow the relationship

$$A_k = \sqrt{2S(\omega_k)\Delta\omega} \tag{6.10}$$

where $\Delta\omega$ is a constant difference between the frequencies. The amplitude function in Equation (6.10) was further used to compute wave-induced responses in the time domain in the simulations. However, as described by Faltinsen [26], the actual heave motion of the rig depends on the response amplitude operator (RAO) spectrum. The responding motion of the rig is dependent on the frequency of the incoming waves, which is illustrated in Figure 6.6 where the rig response spectrum $R(\omega)$ is given by

$$R(\omega) = S(\omega)RAO(\omega)^2. \tag{6.11}$$

The RAO spectrum that was used in this work was based on values from the Aker H6e semi-submersible for ultra deep water and harsh environ-

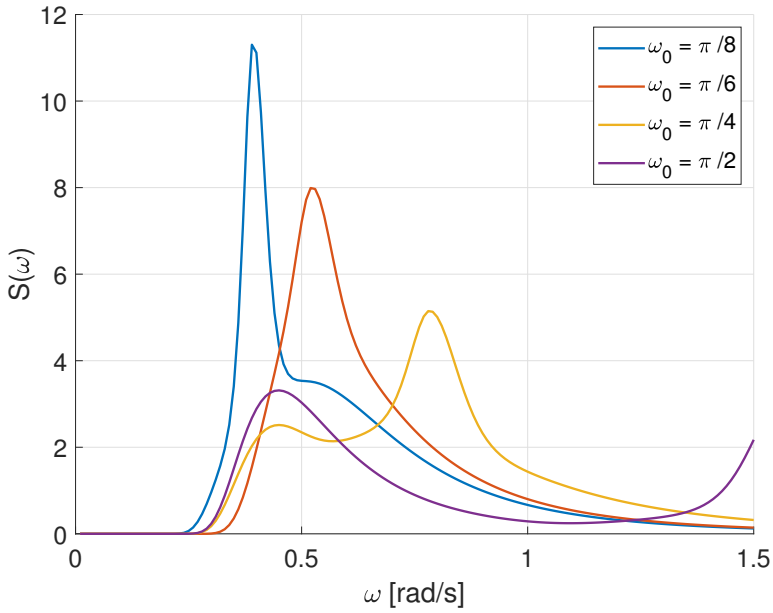

Figure 6.5: Thorsethaugen spectrum with a set of peak frequencies, $H_s = 6$ m.

ment. The responding heave amplitude of the rig is greatest for incoming waves with a period range of 10-15 seconds. In the simulator, the frequency range is divided up in an equidistant grid of N frequencies where the wave frequency vector $\omega = [\omega_1, \omega_2, ...\omega_N]$ was used in superposition to get the heave motion z_{rig} of the rig. The vertical position of the rig can be calculated as

$$z_{rig}(t) = \sum_{k=1}^{N} \sqrt{2R(\omega_k)\Delta\omega} \sin\left(\omega_k t + \phi_k\right), \tag{6.12}$$

where ϕ_k was generated randomly from a uniform distribution on the interval $[0, 2\pi]$ in the simulator.

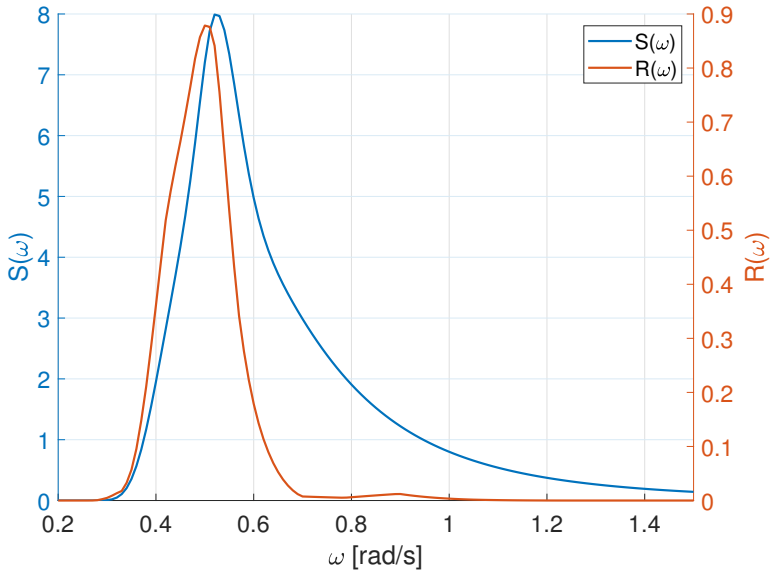

Figure 6.6: Thorsethaugen spectrum and RAO with $H_s = 6$ m and $\omega_0 = \frac{2\pi}{12}$ rad/s.

6.4 Tripping reference

In order to accomplish a smooth acceleration of the drill string, a calculation of an appropriate tripping velocity trajectory is necessary. Consider the following sigmoid function as a candidate for this reference trajectory,

$$v_r(t) = \begin{cases} \frac{\hat{v}_r}{1+e^{k(t_0-t)}}, & \text{if } t_1 > t > t_0 \\ \hat{v}_r, & \text{if } t_2 > t > t_1 \\ \frac{\hat{v}_r}{1+e^{-k(t_0-t)}}, & \text{if } t_3 > t > t_2 \end{cases} \tag{6.13}$$

where $\hat{v}_r$ is the peak tripping velocity. The reference trajectory is displayed in Figure 6.7, where the different time indices in Equation (6.13) are indicated. This reference trajectory was considered due to the smoothness of the sigmoid function, both in the beginning of the acceleration and when the velocity approaches $\hat{v}_r$. It is also a simple function to implement in software, and it has a deterministic acceleration, adjustable by the coefficient

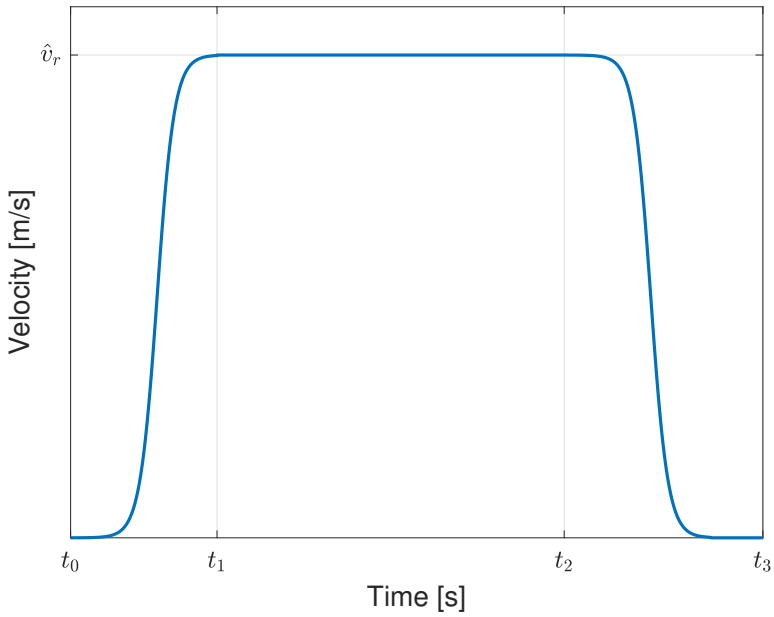

Figure 6.7: Tripping velocity reference, $v_r(t)$.

k. Other tripping references were tried out, e.g. reference trajectories generated by a reference model based on the hoisting system model in chapter 2. The simoid function was favorable because of the simple acceleration adjustment. The necessary tripping acceleration and jerk was calculated by taking the respective time derivatives of the tripping velocity reference in Equation (6.13). In addition, the algorithm that was generating the tripping reference was implemented such that the total tripping distance was equal to the length of one stand. This was formulated as an equality constraint where the integrated tripping velocity had to be equal to the length of a stand, denoted L_{ds}. Mathematically, this can be expressed as

$$\int_{t_0}^{t_3} v_r(t)dt = L_{ds}. \tag{6.14}$$

With the system inputs discussed in this chapter, the system will be simulated with several tripping scenarios in the next chapters.

Chapter 7

Simulations

In this chapter, a simulation of a tripping operation with the active heave compensation system will be presented, as well as a simulation utilizing the conventional tripping method will be covered. The simulations carried out in this chapter will be the foundation for the discussions given in chapter 8.

7.1 System overview

Before the simulations are presented, a block diagram overview of the system can be viewed in Figure 7.1. The blocks in the control strategy part of the figure were covered in chapters 5 and 6, whereas the blocks in the physical part were covered in chapters 2 and 3. In addition, an overview of the system variables is given in Table 7.1.

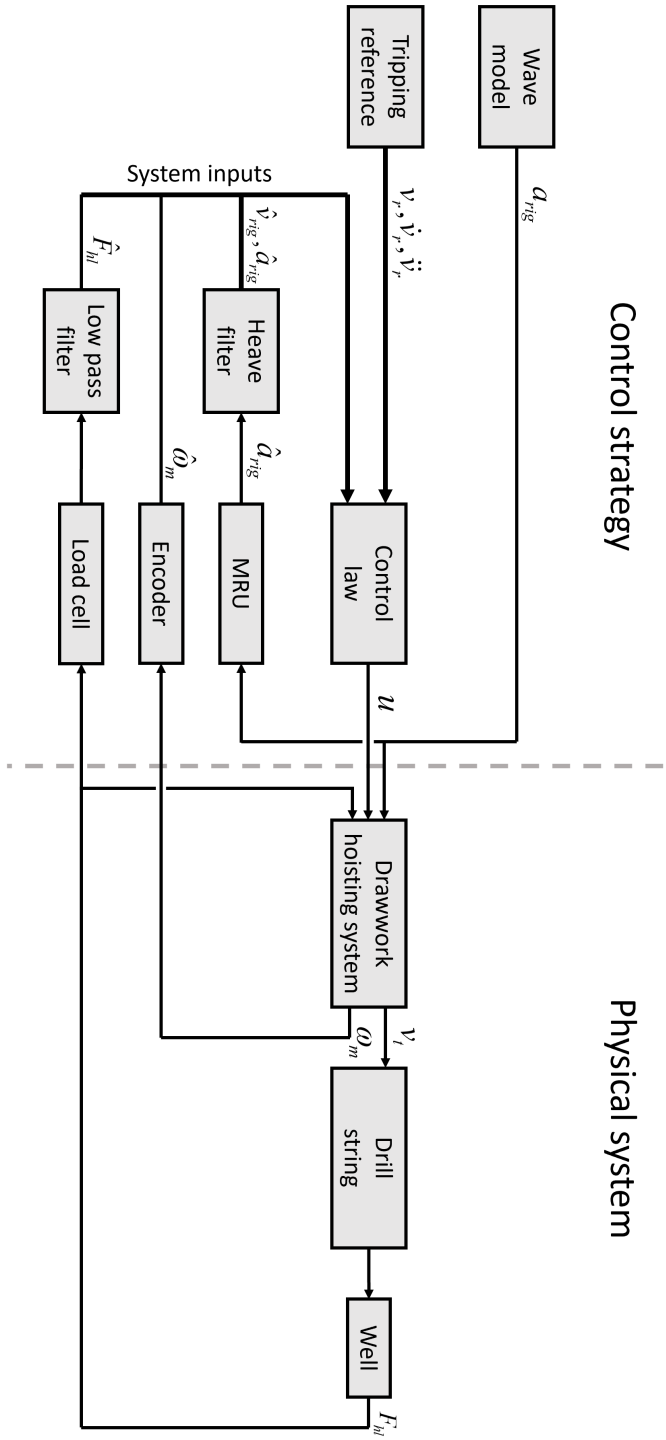

Figure 7.1: Block diagram of the control strategy and the physical system.

v_t	Tripping velocity
$\hat{v}_t$	Estimated tripping velocity
v_r	Tripping velocity reference
z_{rig}	Rig heave position
v_{rig}	Rig heave velocity
$\hat{v}_{rig}$	Estimated rig heave velocity
a_{rig}	Rig heave acceleration
$\hat{a}_{rig}$	Estimated rig heave acceleration
z_{bit}	Position of drill bit
v_{bit}	Velocity of drill bit
P_m	Motor power consumption
ω_m	Motor angular velocity
i_a	Motor amperage
u	Control input, motor voltage
p_{bh}	Pressure bottom hole
F_{hl}	Hook load

Table 7.1: System variables table.

7.2 Simulations

In the forthcoming simulations, an upward tripping operation of a 30 meter long drill string stand was performed. The tripping velocity was set according to the validation data set in chapter 4, i.e. 1 meter per second. The significant wave height was set to 6 meters, where the same set of waves was used in each simulation. A list of the main simulation parameters is given in Table 7.2. At the start of each simulation, the states got 2 seconds to settle before the recording started, as part of an equilibrate regime. After numerous test simulations, the tripping acceleration was limited to 0.25 m/s^2, as it resulted in a non-oscillatory hook load. Simulations with too aggressive tripping acceleration resulted in pressure waves propagating in the steel of the drill string, rendering the hook load measurements too jittery for use in the controller. Furthermore, a high tripping acceleration resulted in an amplification of the pressure oscillations down hole. A more compre-

hensive analysis of the tripping acceleration is given in chapter 8.

Δt	0.01 s	Simulator time step
f_m	10 Hz	Update frequency in encoder
f_{mru}	10 Hz	Update frequency in MRU
f_{hl}	4 Hz	Update frequency in load cell
f_c	10 Hz	Update frequency in controller
ω_b	8 rad/s	Controller band width
ζ	1	Controller relative damping coefficient
η_m	0.01 rad/s	Standard deviation encoder
η_{rig}	0.01 m/s^2	Standard deviation MRU
η_{hl}	3 kN	Standard deviation load cell
H_s	6 m	Significant wave height
T_0	12 s	Peak wave period
$\dot{\hat{v}}_r$	0.25 m/s^2	Peak tripping acceleration reference
$\hat{P}_m$	2600 kW	Power rating on the drawwork motor

Table 7.2: Simulation parameter table.

Two simulations will be presented in this section. The heave compensation system derived in this work was used for active hoisting in the first simulation. The control law derived in chapter 5 was tuned such that the response of the drill string was sufficiently fast, but not oscillatory. Setting the controller gains too high resulted in drill string oscillations. In addition, the measurement noise started influencing the performance of the controller. Furthermore, an anti windup strategy was implemented to better handle situations with saturated control input. In the second simulation, the control system was not correcting for wave-induced heave motion of the rig. The control input was set directly based on the tripping reference, without any motion control.

7.2.1 Active hoisting simulation

In this simulation, the active heave compensation system was utilized in the tripping operation. The simulation results are presented in Figure 7.2 and 7.3. The tripping velocity reference can be viewed in Figure 7.2a together with the true and estimated velocity of the drill string. One may observe that the velocity of the drill string was slightly negative for $t = 0$ s. This is due to the weight of the drill string accelerating it in the negative heave direction during the equilibrate phase. As the drill string was accelerated towards the peak tripping velocity, it was very accurate with respect to the reference. During the constant tripping velocity phase of the plot, i.e. for $t = 15$ seconds through $t = 35$ seconds, the majority of the wave-induced heave motion was compensated for by the control system. However, one may observe that the drill string response was a bit slow as it converged to the peak velocity. Higher control gains were also simulated, but yielded a less stable response. The heave motion of the rig is displayed in Figure 7.2b and 7.2c.

In Figure 7.2c, the performance of the heave filter may be observed while it was estimating the heave velocity of the rig. The slight overshoot by the filter from $t = 30$ seconds to $t = 35$ seconds caused the controller to overshoot slightly, as displayed in Figure 7.2a. However, this overshoot did not induce any major pressure oscillations in the well. One may notice that the estimated heave velocity is slightly lagging the true velocity of the rig. This is caused by the finite update frequency of the accelerometer, and the time consumption in the filter computations. However, this time lag is sufficiently short in comparison to the period of the waves, so no major performance issues were caused by this.

Further, in Figure 7.3a, the power consumption of the drawwork motor is displayed. It is clear that some of the measurement noise was propa-

gating through the controller, resulting in some jitter on the control input. However, these high frequency oscillations were damped out through the dynamics of the motor, leaving the performance of the control system unaffected. One may also notice that the power consumption peaked at approximately 1500 kilowatts, occurring as the rig descended rapidly. This is approximately 60 % of the total capacity of the drawwork motor.

Moving along to Figure 7.3b, the pressure down in the well hole is plotted relative to the static pressure. As the drill string was accelerated out of the well, the resulting decompression reduced the pressure around the drill bit. This resulted in a pressure drop, as displayed in the figure. After the hoisting system had accelerated the drill string, one may observe some pressure oscillations with initial amplitude of approximately 0.45 bar. These oscillations were damped out over time. The frequency of these oscillations does not match the frequency of the waves, because they represent pressure waves that were propagating in the mud down hole. When a drill string is accelerated, the decompression down hole induces pressure waves that propagate in the fluid below the drill bit. These pressure waves are reflected in the bottom of the well, resulting in these periodic oscillatory pressure waves seen in the figure.

In Figure 7.3c, one may observe the total vertical depth of the drill bit. Notice that the drill bit was elevated approximately 30 meters during the simulation, which is the length of one drill string stand. Lastly, in Figure 7.3d, the measured hook load is displayed. As the drill string was simulated with elastic properties, hook load oscillations may occur if the movement of the drill string approaches its natural frequency. This did not happen in this simulation, since the impact of the periodical wave motion was minimized by the heave compensation system.

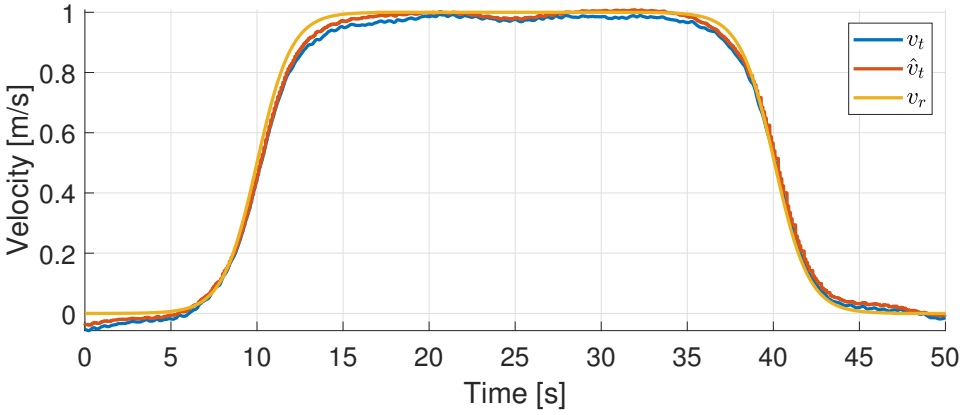

(a) True, estimate and reference tripping velocity of the drill string.

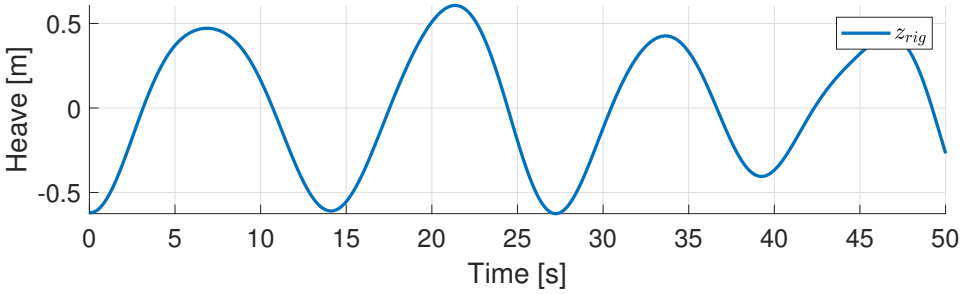

(b) Heave position of the rig.

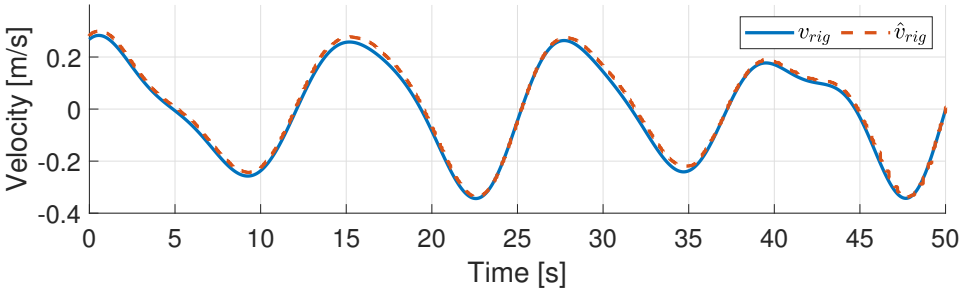

(c) True and estimated heave velocity of the rig.

Figure 7.2: Active hoisting simulation with $H_s = 6$ m and $\hat{v}_r = 1.0$ m/s. Part 1/2.

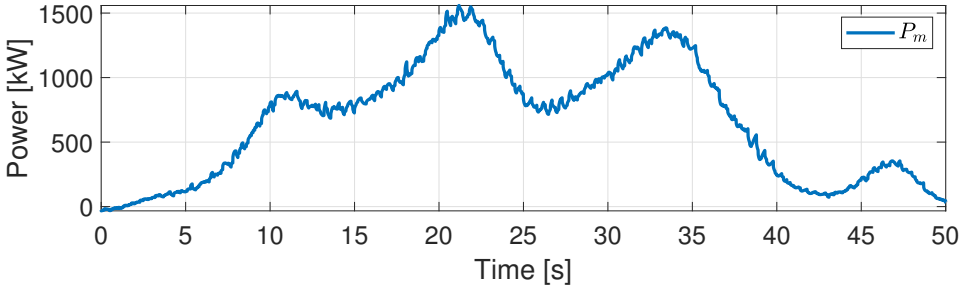

(a) Power consumption of the drawwork motor.

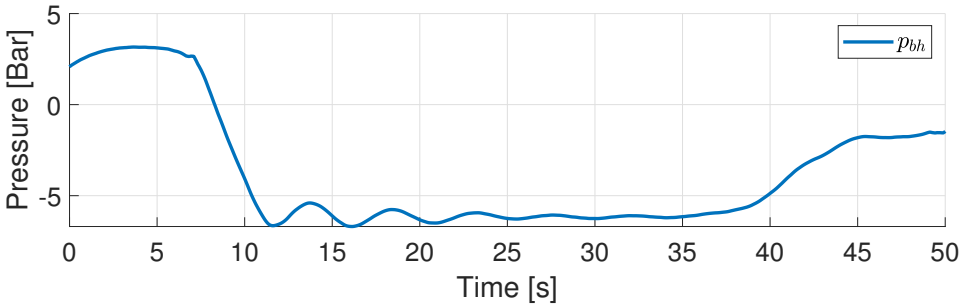

(b) Pressure in the bottom of the well relative to the static pressure.

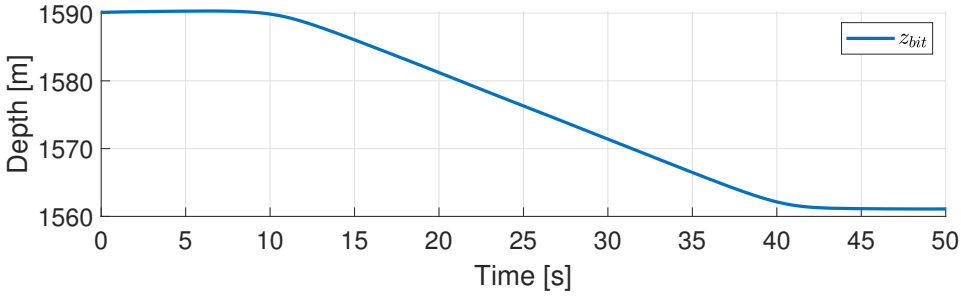

(c) Depth of the drill bit.

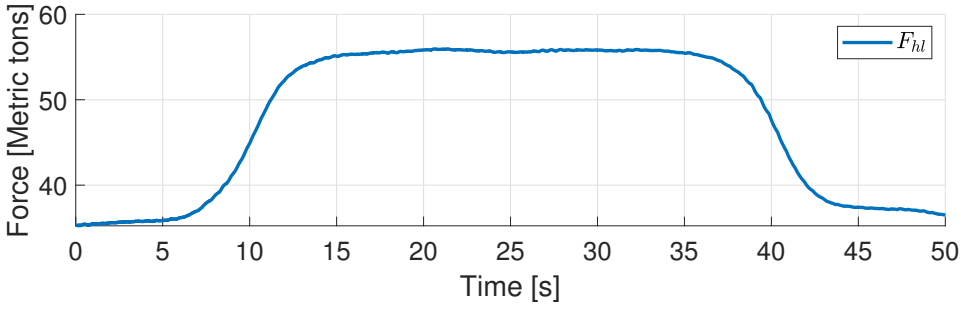

(d) True and estimated hook load.

Figure 7.3: Active hoisting simulation with $H_s = 6$ m and $\hat{v}_r = 1.0$ m/s. Part 2/2.

7.2.2 Constant hoisting simulation

In this simulation, the motor voltage control input was tracking the tripping velocity reference, without any heave compensation control. I.e., the tripping velocity was controlled relative to the heave velocity of the rig. In order to make the comparison clear, the same tripping velocity reference and the same set of waves were used in this simulation as with the active hoisting.

The results from the simulation are displayed in Figure 7.4 and 7.5. As one may observe in Figure 7.4a, the velocity of the drill string was significantly influenced by the wave-induced heave motion. As the reference tripping velocity approached 1 meter per second, the drill string velocity overshot the reference by 40 %. While the tripping reference was constant, the velocity of the drill string oscillated with the waves. This oscillation continued throughout the simulation, as there was no active heave compensation controller counteracting the heave motion of the rig. Figure 7.4b and 7.4c display the heave motion of the rig, which is equivalent to the previous simulation.

Further, in Figure 7.5a, the power consumed by the drawwork motor is displayed. As opposed to the previous simulation, the power draw was a lot smoother with constant hoisting, as no noise contaminated measurements were influencing the motor voltage. Furthermore, the power required for constant hoisting was very similar to the previous simulation with active hoisting.

The pressure down hole is shown in Figure 7.5b. The pressure dropped as expected when the drill string started accelerating out of the hole. The same type of pressure oscillations occurred when the reference became constant. However, by inspection, one may observe that these pressure oscillations had a greater amplitude compared to the previous simulation. To be spe-

cific, the pressure oscillated with an amplitude of 1.8 bar, opposed to the 0.45 bar observed in the active hoisting simulation. This difference is interesting, and will be further discussed in the next chapter.

The depth of the drill bit is displayed in Figure 7.5c, where one may notice some minor oscillations as the bit was moving towards the surface. Lastly, the hook load displayed in Figure 7.5d was also affected by the heave motion of the rig. However, the frequency of the waves was not close enough to its natural frequency for any major amplification of the oscillations.

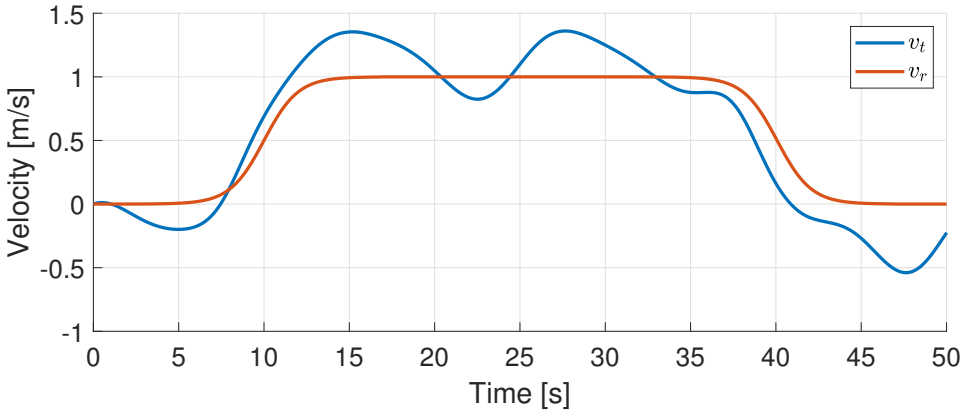

(a) True and reference tripping velocity of the drill string.

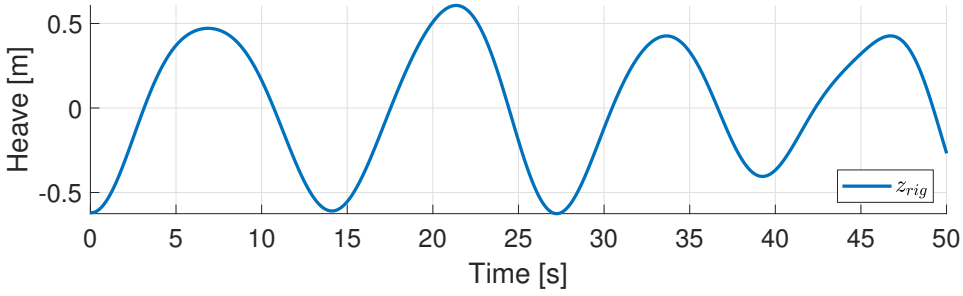

(b) Heave position of the rig.

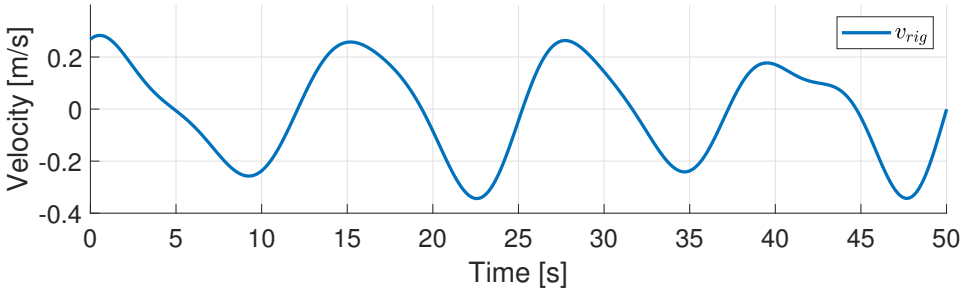

(c) Heave velocity of the rig.

Figure 7.4: Constant hoisting simulation with $H_s = 6$ m and $\hat{v}_r = 1.0$ m/s. Part 1/2.

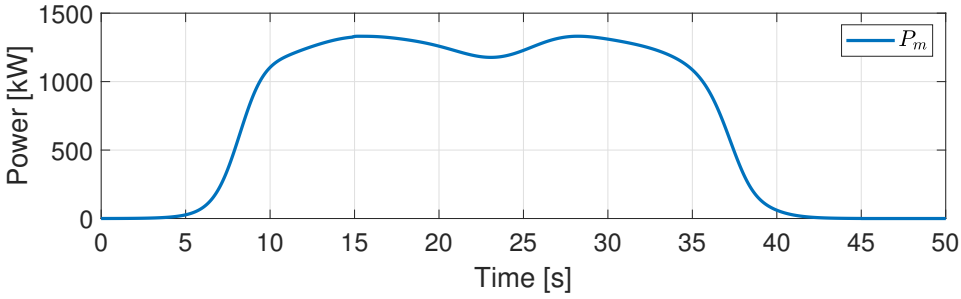

(a) Power consumption of the drawwork motor.

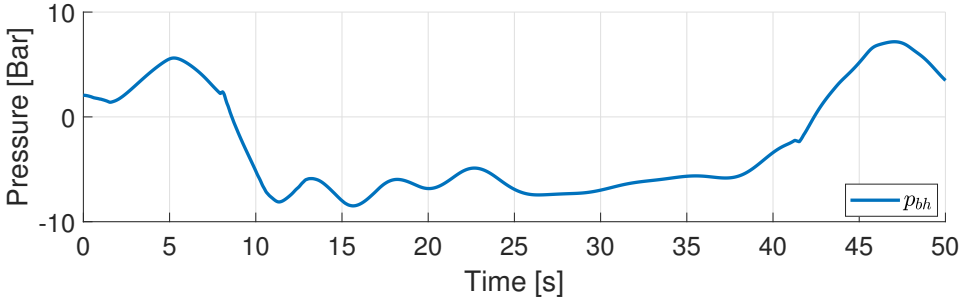

(b) Pressure in the bottom of the well relative to the static pressure.

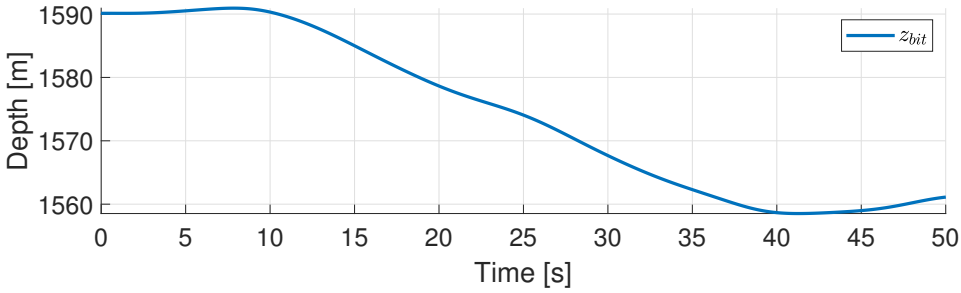

(c) Depth of the drill bit.

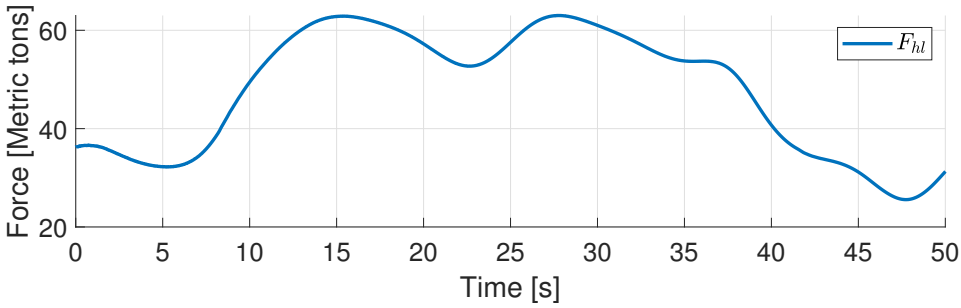

(d) Hook load.

Figure 7.5: Constant hoisting simulation with $H_s = 6$ m and $\hat{v}_r = 1.0$ m/s. Part 2/2.

Chapter 8

Discussion

In this chapter, a discussion on the performance of the active heave compensation system will be presented. The pressure oscillations down hole will be the primary topic of the following discussions. In addition, a discussion will be given on how different wave heights, and tripping configurations alters the performance of the active hoisting system.

8.1 Heave compensated position control

As discussed in the introduction of this thesis, there are multiple heave compensation techniques that are used for constant positioning of the drill bit, when there is no tripping involved. In order to compare the heave compensation ability of the active hoisting system to other methods, a small analysis on the performance of the hoisting system is given, where the velocity reference was set to zero. Motivated by the work of Strecker et al. [5], the following measure for oscillations down hole is proposed. For a given significant wave height, let χ be the probability for the pressure down hole p_{bh} to exceed rms(p_{bh}) by a factor of γ or more. Mathematically, this may

be expressed as

$$\chi(\gamma) = \text{prob}\left(|p_{bh}| > \gamma \cdot \text{rms}(p_{bh})\right). \tag{8.1}$$

Here, the rms() function is the *root mean square* of the time series, expressed as follows for a general time series defined by $f(t)$.

$$\text{rms}(f(t)) = \sqrt{\frac{1}{T_2 - T_1}\int_{T_1}^{T_2} f(t)^2 dt} \tag{8.2}$$

In Figure 8.1, the probability χ is plotted as a function of γ for three different significant wave heights. For the simulation with significant wave height of 6 meters, the majority of the oscillation peaks have a lower value than the calculated rms. However, the pressure oscillations in the simulations with higher waves exceed their respective rms values more than 20 % of the time. The simulation results show a slight improvement on the oscillation damping abilities of the active hosting system upon comparison with other control strategies discussed by Strecker et al. [5]. For a numerical summary of the data used in the figure, one may draw attention to Table 8.1.

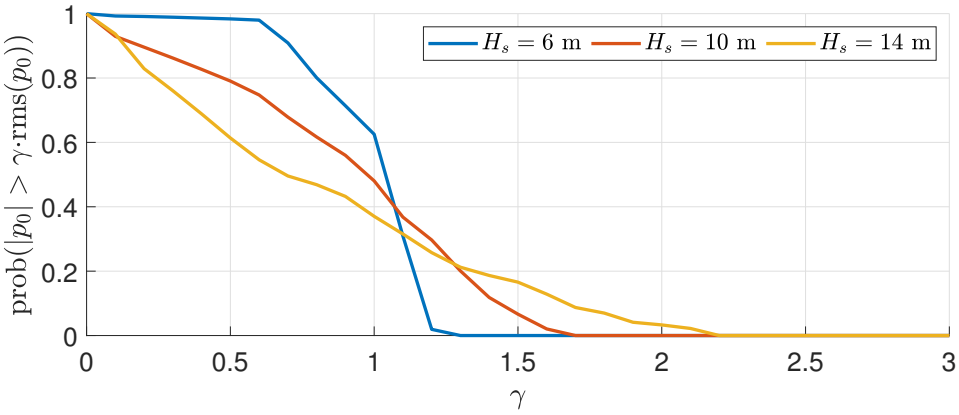

Figure 8.1: Plot of pressure oscillation amplitudes versus rms for different significant wave heights.

	$H_s = 6$ m	$H_s = 10$ m	$H_s = 14$ m
prob($\|p_{bh}\| > 1 \cdot \text{rms}(p_{bh})$)	16.18 %	22.32 %	26.81 %
prob($\|p_{bh}\| > 1.5 \cdot \text{rms}(p_{bh})$)	0.00 %	2.17 %	8.48 %
prob($\|p_{bh}\| > 2 \cdot \text{rms}(p_{bh})$)	0.00 %	0.00 %	1.11 %

Table 8.1: Table of pressure oscillation amplitudes versus rms for different significant wave heights.

8.2 Heave compensated tripping

In this section, simulations with active tripping will be compared to tripping with constant velocity for a set of system configurations. According to Vikebø et al. [27], the maximum significant wave height in the north sea ranges from 6 meters to 14 meters. Hence, this was the range of significant wave heights that was simulated. In order to make the comparison between the different simulations clear, the same set of waves generated with a specific significant wave height were used in each simulation with that respective sea state.

8.2.1 Pressure drop down hole

As mentioned in the previous chapter, there will always be a pressure drop down hole due to the decompression that occurs when the drill string is moving out of the well. Furthermore, this pressure drop increases for greater tripping velocities, as displayed in Figure 8.2. Here, one may observe the pressure down hole during tripping with three different tripping velocities, where the wave height was set to zero. This pressure drop is inevitable unless drilling mud is injected into the well as the drill string is hoisted out, equilibrating the decompression. Since this can be done with standard drilling equipment such as the mud pump, the performance of the control system will be gauged based on the pressure oscillations down hole

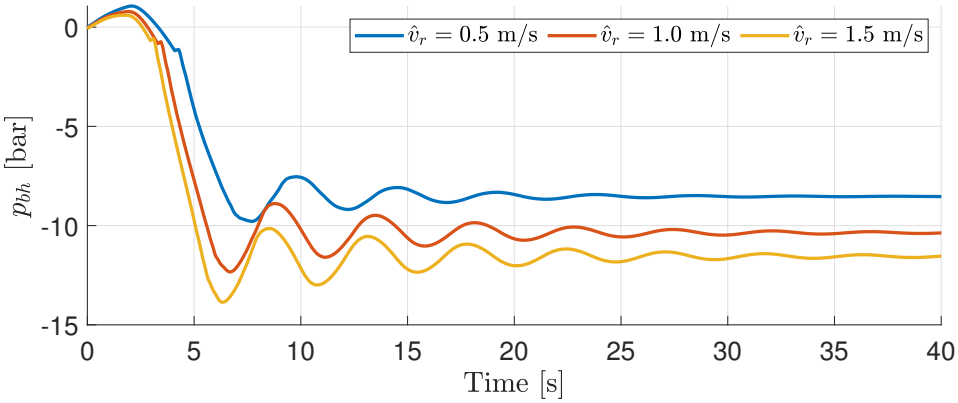

Figure 8.2: Pressure in the bottom of the well relative to the static pressure during tripping with a set of velocities. The wave height was set to zero in these simulations.

that follows after the decompression.

8.2.2 Pressure oscillations down hole

Next, the performance of the active hoisting system will be discussed for a range of tripping velocities, accelerations, and significant wave heights. As discussed in the previous section, the performance of the control system will be gauged based on the oscillations down hole. Specifically, two performance measures will be presented in this work in order to compare the performance of the active hoisting system to the conventional tripping method. The first performance measure will give an indication on the magnitude of the pressure oscillations, whereas the second performance measure will give an indication on the persistence of these oscillations. Both the magnitude and the persistence of the pressure oscillations may cause fatigue to the structural integrity of the well. Furthermore, utilizing both methods will give a richer image of how the performance of the heave compensation system is altered by the different sea states and tripping trajectories.

Pressure oscillation magnitude

First, the performance measure that encapsulate the magnitude of the pressure oscillations will be discussed. Let Δp_{bh} be the pressure difference between the maximum pressure and the minimum pressure that occurred down hole during a tripping operation. Mathematically, this delta pressure is expressed as follows,

$$\Delta p_{bh} = \max_{t \in [t_1, t_2]} p_{bh}(t) - \min_{t \in [t_1, t_2]} p_{bh}(t), \tag{8.3}$$

where $p_{bh}(t)$ is the pressure down hole as a function of time. Note that the delta pressure will be calculated based on the pressure time series where the tripping reference is constant, i.e. from $t = t_1$ through $t = t_2$, as displayed in Figure 6.7. Thus, the pressure drop previously mentioned will not influence the calculations.

As one may expect, the oscillations down hole were amplified for increasing wave heights when constant hoisting was simulated. In Figure 8.3, the resulting delta pressure from several simulations is displayed. Each simulation was set up with a specific significant wave height, and tripping velocity. In addition, each setup was simulated with both active hoisting, and constant hoisting. Consider Figure 8.3b, where the tripping velocity was set to 1 meter per second, like the simulations previously discussed in this chapter. Yet again, it is clear that tripping with constant hoisting induces a greater delta pressure compared to tripping with active heave compensation. Indeed, this is the case for all the simulated wave heights in this figure. Since the wave height is a stochastic variable, the delta pressure is not strictly increasing as a function of the significant wave height. However, there is a trend of increasing delta pressure for increasing significant wave height. In the active hoisting simulations, the delta pressure did not increase in the same rate as with constant hoisting. Up until significant wave height

of 10 meters, the delta pressure was generally lower than 1 bar. The main reason for the steady increase in delta pressure in the simulations with active hoisting, is the system's inertia. The heave velocity of the rig increases proportionally to the height of the waves. Hence, larger waves demand a faster response of the heave compensation system in order to isolate the drill string from these motions. However, since the measurements are updated at a finite frequency, and the inertia in the hoisting system require time to accelerate, the delta pressure increase slightly for increasing wave heights. In the simulation with the significant wave height of 14 meters, the constrains of the drawwork system came to display, as the necessary lifting power exceeded the capabilities of the drawwork motor. This resulted in a small heave motion of the drill string, which increased the delta pressure to approximately 2 bar.

Next, consider Figure 8.3c, where simulations with a tripping velocity of 1.5 meters per second is displayed. Similarly to the previous plot, the constant hoisting induced greater pressure oscillations down hole than the active hoisting. As the wave height escalated, a more dramatic consequence of the saturated motor came to display when utilizing the active heave control system. In the simulation with significant wave height of 14 meters, the delta pressure reached 5.7 bar. Once again, it is clear that the capacity of the drawwork is limited. However, the capabilities of the drawwork motor will be designed for the conditions where the specific rig is located.

Further, in Figure 8.3a, the delta pressure is plotted for a tripping velocity of 0.5 meter per second. The constant hoisting simulations differ from the other simulations discussed so far. As one may notice, the delta pressure increased rapidly as the significant wave height escalated, resulting in a delta pressure of approximately 20 bar with the greatest waves. At first, this might seem counter-intuitive. However, the downside of tripping at such low velocities is the fact that the drill string will regularly become sta-

tionary. When the rig moves downwards with a wave, the heave velocity of the rig may match this movement, or even surpass the tripping velocity of the drill string. This results in a stationary drill string with respect to the sea bed, stopping the flow of the drilling fluid below the drill bit. Since the mud in the simulator was configured based on a non-Newtonian mud with the Herschel-Bulkley rheological model, the delta pressure necessary to get the mud flowing is quite significant in comparison with the previously discussed pressure oscillations. Hence, these simulations encourage a tripping velocity that exceeds the maximum expected heave velocity when constant tripping is used.

The delta pressures that were used in the figures are shown in Table 8.2. The simulations with tripping velocity of 1 meter per second show an average reduced delta pressure by a factor of approximately six, when comparing the active to the constant hoisting.

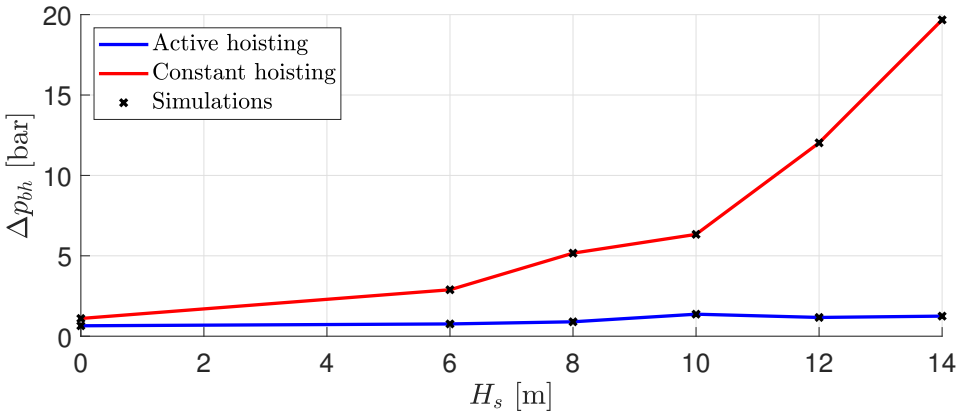

(a) $\hat{v}_r = 0.5$ m/s.

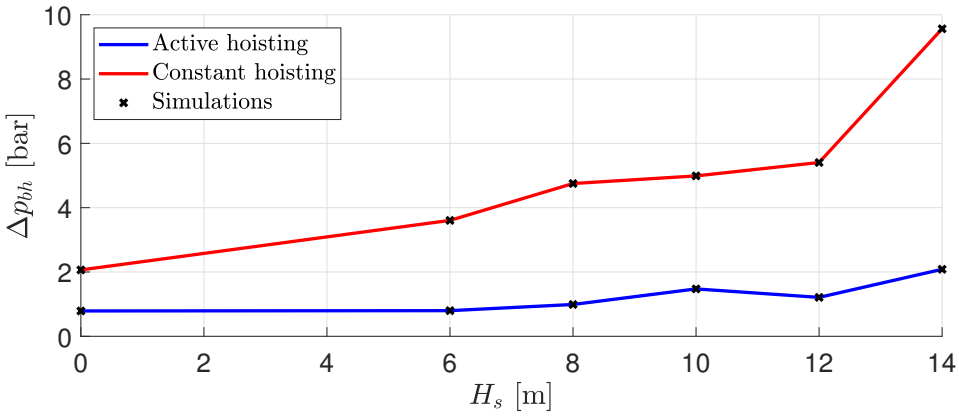

(b) $\hat{v}_r = 1.0$ m/s.

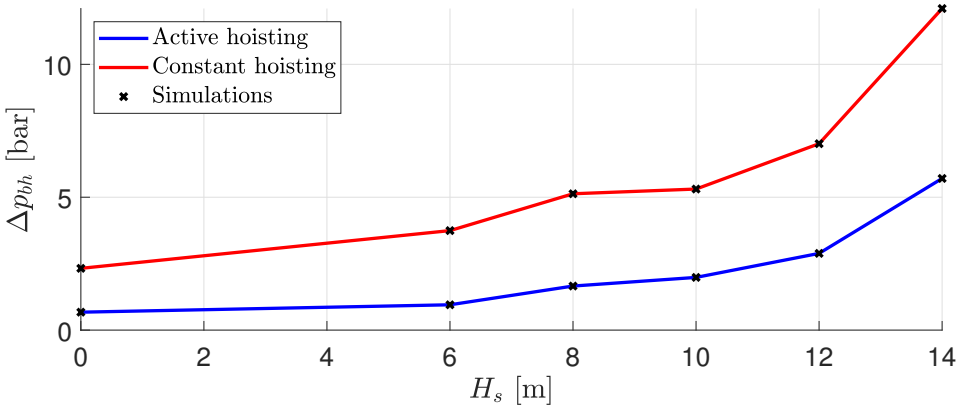

(c) $\hat{v}_r = 1.5$ m/s.

Figure 8.3: Delta pressure down hole with active and constant hoisting, simulated with a range of tripping velocities and significant wave heights.

$\hat{v}_r$	H_s	Δp_{bh}, Active hoisting	Δp_{bh}, Constant hoisting
0.5	0	0.65 bar	1.10 bar
0.5	6	0.76 bar	2.89 bar
0.5	8	0.90 bar	5.17 bar
0.5	10	1.37 bar	6.33 bar
0.5	12	1.17 bar	12.0 bar
0.5	14	1.25 bar	19.7 bar
1.0	0	0.78 bar	2.06 bar
1.0	6	0.79 bar	3.60 bar
1.0	8	0.99 bar	4.75 bar
1.0	10	1.47 bar	4.99 bar
1.0	12	1.21 bar	5.40 bar
1.0	14	2.08 bar	9.56 bar
1.5	0	0.67 bar	2.32 bar
1.5	6	0.95 bar	3.74 bar
1.5	8	1.66 bar	5.13 bar
1.5	10	1.99 bar	5.30 bar
1.5	12	2.89 bar	7.01 bar
1.5	14	5.71 bar	12.1 bar

Table 8.2: Table of delta pressure down hole with active and constant hoisting, simulated with a range of tripping velocities and significant wave heights.

Next, the delta pressure performance measure will be used to analyse the performance when altering the tripping acceleration. Consider Figure 8.4, where the resulting delta pressures from active hoisting simulations with several tripping accelerations are displayed. Each simulation in this figure was configured with a significant wave height of 6 meters, and a tripping velocity of 1 meter per second. As previously discussed, the delta pressure is caused by viscous drag induced by motion of the drill string. According to Munson et al. [28], viscous drag is assumed to be linearly proportional to the velocity of the fluid for low velocities. Hence, one may assume that the viscous drag is quadratic proportional to drill string acceleration. Based

on this assumption, the delta pressures from the simulations were used to curve fit a 2nd order polynomial by regression. As the curve suggests, the benefit of reducing the tripping acceleration further from the 0.25 m/s^2 used in the simulations previously discussed is minimal. Furthermore, in a practical setting where the well might be containing long horizontal sections, the acceleration of the drill bit can not be controlled with such precision due to the increased friction force. Hence, the simulations show that a tripping acceleration of 0.25 m/s^2 is sufficiently close to an optimal tripping trajectory.

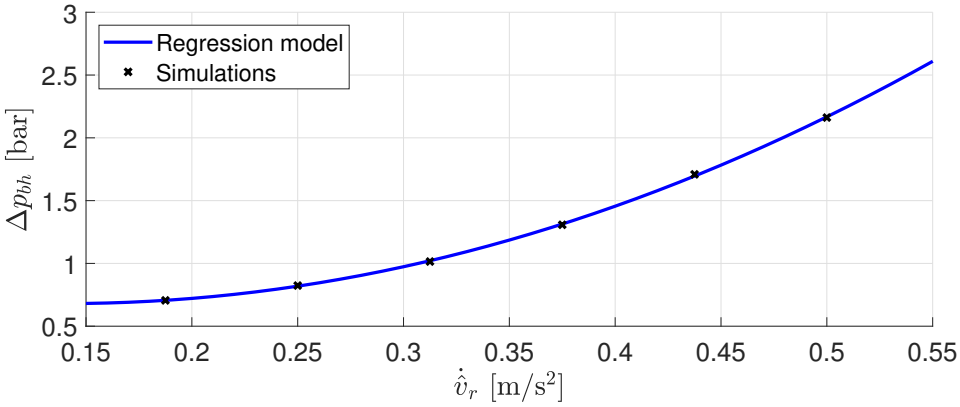

Figure 8.4: Delta pressure down hole as a function of tripping reference acceleration, simulated with $H_s = 6$ m, and $\hat{v}_r = 1.0$ m/s.

Pressure oscillation persistence

Additionally to the delta pressure, a second performance measure was used to validate the active hoisting system. This measure encapsulates the pressure oscillations caused by wave-induced heave motion of the rig, accumulated over time. Let $\tilde{p}_{bh}(t)$ be the simulated pressure down hole for a given tripping velocity, where no waves were influencing the movement of the rig. If one compare such a simulation to a simulation with wave-induced

pressure oscillations, one may discover that the pressure oscillations persist when adding a sea state. An example of this is displayed in Figure 8.5, where the pressure down hole is plotted with and without waves for a controlled tripping operation of 1 meter per second. Notice that the pressure oscillations for $\tilde{p}_{bh}(t)$ got damped out over the course of the simulation, whereas the pressure oscillations persisted throughout the simulation when waves were influencing the rig. However, the difference in delta pressures is negligible. Therefore, a second performance measure is necessary to capture these persistent oscillations.

Let υ be the *root mean square* of the difference between the pressure time series simulated with a given sea state, and the case with no waves.

$$\upsilon = \text{rms}(p_{bh}(t) - \tilde{p}_{bh}(t)) \tag{8.4}$$

Thus, the greater the persistent oscillations are, the greater will the value of the performance measure be. In Figure 8.6, the same set of simulations as the first performance measure is displayed for υ. Similarly to the observed delta pressure previously discussed, the persistence of the pressure oscillations increases for greater wave heights. As expected, the controlled tripping operations yielded less pressure oscillations than the tripping operations utilizing the conventional method. However, there was a notable difference in pressure oscillations between the controlled tripping with velocity of 1 meter per second and 1.5 meter per second. It is clear that the saturation of the hoisting system not only induced higher pressure peaks, but also induced oscillations that persist over time. Further, the constant hoisting simulations confirm the previously discussed discovery that the pressure oscillations related to the low tripping velocity of 0.5 meter per second cause worse condition down hole.

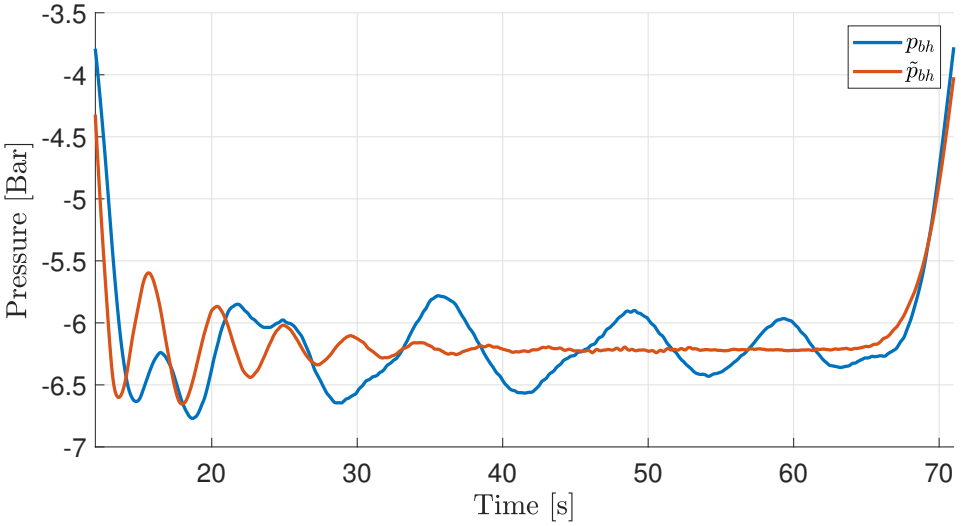

Figure 8.5: Pressure down hole with and without waves. p_{bh} was simulated with significant wave height of 8 meters. Both simulated with a tripping velocity of 1 meter per second.

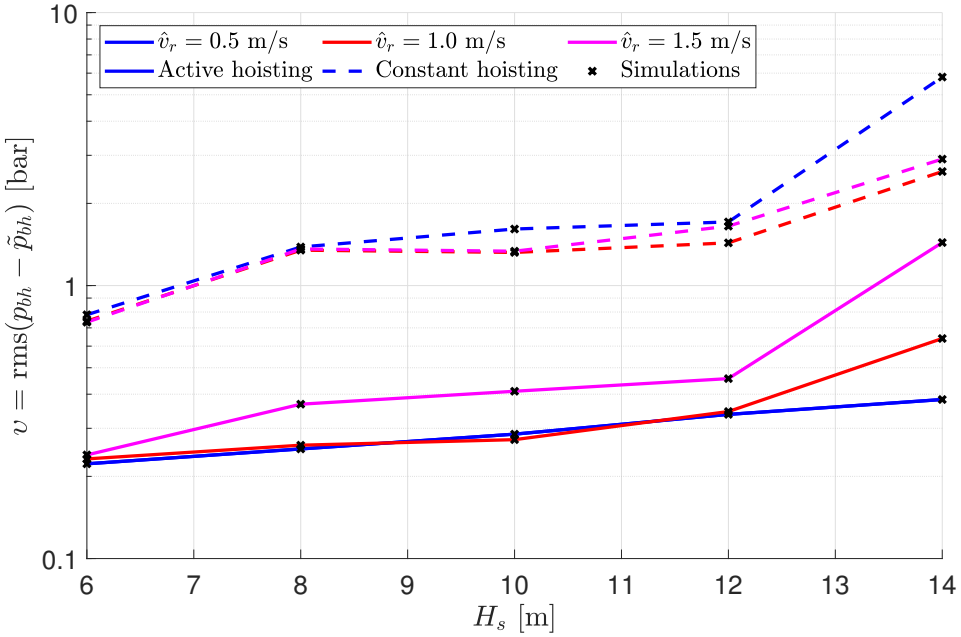

Figure 8.6: *Root mean square* of the difference in down hole pressure with and without waves for a set of tripping velocities and significant wave heights.

Chapter 9

Conclusion

Several simulations were carried out in this work, combining a variety of sea states and tripping reference trajectories. Based on simulations of the models derived in this study, the wave-induced pressure oscillations that occur down hole during tripping, may be reduced by a factor of about six if an active heave compensation system is utilized. This may be accomplished if a control system is designed to combine the standard mud injection methods with active hoisting, yielding pressure wave amplitudes down to 0.4 bar. Furthermore, the pressure oscillations are highly correlated to both the tripping velocity and acceleration. Slow tripping where the drill string may become stationary due to the relative velocity of the waves may amplify pressure waves when non-Newtonian fluids are involved. Moreover, tripping too fast induces greater pressure wave amplitudes down hole due to the increased flow rate. This study shows that an optimal tripping trajectory with correct velocity and acceleration will indeed reduce the amplitude of pressure wave oscillations down hole.

Simulations also revealed the importance of a sufficiently powerful hoisting system that is capable of following the wave-induced heave motion of

the rig during rough sea states. Saturating the system may result in rapid accelerations of the drill string, inducing pressure waves both down hole, as well as in the structure of the drill string.

The results in this study are based on simulations of models that represent simplified dynamics. Even though the simulations show aspects that are important in order to minimize pressure variations in a well, the methods should be examined further in practice to validate the results.

Chapter 10

Suggestions for future work

The scope of this work has been to address an active hoisting system strategy to minimize pressure oscillations in a well. This thesis contains several simulations with different tripping trajectories to be applied to the active hoisting system. However, the reference was found by manual trial and error. An optimization strategy could be developed in future work where an optimal tripping reference was calculated, minimizing the pressure oscillations for a given sea state. In addition, future work could develop a control strategy combining a managed pressure drilling strategy, e.g. the strategy derived by Strecker et al. [5], together with the active hoisting control design derived in this work.

Bibliography

[1] B.A. Foss J.G. Balchen, T. Andresen. *Reguleringsteknikk, 5. utgave*. Institutt for teknisk kybernetikk, NTNU, Trondheim, 2003.

[2] J. A. Burkhardt. Wellbore pressure surges produced by pipe movement. *Society of Petroleum Engineers. doi:10.2118/1546-G-PA*, 1961.

[3] O. Breyholtz, G. Nygaard, J. Godhavn, and E. H. Vefring. Evaluating control designs for co-ordinating pump rates and choke valve during managed pressure drilling operations. *2009 IEEE Control Applications, (CCA) Intelligent Control, (ISIC)*, pages 731–738, 2010. ISSN 1085-1992. doi: 10.1109/CCA.2009.5281013.

[4] Gerhard Nygaard Øyvind Breyholtz and Michaeal Nikolaou. Automatic control of managed pressure drilling. *Published in: Proceedings of the 2010 American Control Conference. INSPEC: 11509043*, 2010.

[5] Timm Strecker and Ole Morten Aamo. Attenuating heave-induced pressure oscillations in offshore drilling by downhole flow control. 2017.

[6] Timm Strecker and Ole Morten Aamo. Simulation of heave-induced pressure oscillations in herschel-bulkley muds. *Society of Petroleum Engineers. doi:10.2118/185947-PA*, 2017.

[7] Eric Cayeux and Gunnstein Sælevik. Evaluation of hook-load measurements in drilling rig hoisting systems. *SINTEF-7020384/04/14*, 2014.

[8] National Oilwell Varco. Automated drawwoks system (ads), 2018. URL `https://www.nov.com/Segments/Rig_Systems/Land/Hoisting/Drawworks/Drilling_Drawworks.aspx`.

[9] Roger A. Freedman Hugh. D. Young. *University physics*. Jim Smith, 2012.

[10] Eric Cayeux. On the importance of boundary conditions for real-time transient drill-string mechanical estimations. *Society of Petroleum Engineers. doi:10.2118/189642-MS*, 2018.

[11] O. Egeland and T. Gravdahl. *Modelling and simulation for automatic control*. Marine Cybernetics AS, 2003.

[12] Morten Lie. Heave compensated tripping. *Specialization project, Department of Engineering Cybernetics, NTNU*, 2018.

[13] W.D. Greenfield and A. Lubinski. Use of bumper subs when drilling from floating vessels. *Society of Petroleum Engineers. doi:10.2118/1549-PA*, 1967.

[14] Anders Rønning Dahlen. Modelling the effect of continuous circulation on downhole pressure oscillations caused by rig heaving. *Master thesis, Department of Engineering Cybernetics, NTNU*, 2015.

[15] American Petroleum Institute. *Rheology and Hydraulics of Oil-well Drilling Fluids: Upstream segment*. API, 2006. URL `https://books.google.no/books?id=T3mZMQAACAAJ`.

[16] W.H. Herschel and R. Bulkley. Konsistenzmessungen von gummi-benzollösungen. *Kolloid-Zeitschrift 39 (4): 291-300.https://doi.org/10.1007/BF01432034*, 1926.

[17] R.F. Mitchell. Dynamic surge/swab pressure predictions. *Society of Petroleum Engineers. doi:10.2118/16156-PA*, 1988.

[18] Thor I. Fossen. *Handbook of Marine Craft Hydrodynamics and Motion Control*. John Wiley & Sons, Ltd, 2011.

[19] Seatex Kongsberg. The ideal marine motion sensor, 2018. URL `https://www.km.kongsberg.com`.

[20] R. W. Beard and T. W. Mclain. *Small unmanned aircraft*. Princeton University Press, 2012.

[21] Eric Cayeux and Hans Joakim Skadsem. Accuracy and correction of hook load measurements during drilling operations. *Society of Petroleum Engineers. doi:10.2118/173035-MS*, 2015.

[22] J.-M. Godhavn. Adaptive tuning of heave filter in motion sensor. *174 - 178 vol.1. 10.1109/OCEANS.1998.725731.*, 1998.

[23] M. Richter, K. Schneider, D. Walser, and O. Sawodny. Real-time heave motion estimation using adaptive filtering techniques. *IFAC Proceedings Volumes*, 2014.

[24] K. Thorsethaugen. Model for a doubly peaked wave spectrum. *SINTEF report STF22 A, 96204*, 1996.

[25] Norsok Standard. *Actions and Actions Effects*. Rev. 1.0.N-003, 1999.

[26] O. Faltinsen. *Sea Loads on Ships and Offshore Structures Series Vol 1*. Cambridge University Press, 1993.

[27] Frode Vikebø, Tore Furevik, Gunnar Furnes, and Nils Gunnar Kvamstø. Wave height variations in the north sea and on the norwegian continental shelf, 1881–1999. *Continental Shelf Research 23 (2003) 251–263*, 2002.

[28] Bruce R. Munson, Donald F. Young, Theodore H. Okiishi, and Wade W. Huebsch. *Fundamentals of Fluid Mechanics*. Don Fowley, 2009.

Appendix A

Sheave velocity ratio

In this appendix, the ratio between the rotational velocity of the first sheave and the ith sheave in the block and tackle will be derived. The sheaves rotate with different velocity relative to each other, so in order to find a generalization of this ratio, one may consider an example setup.

Let there be $n_l = 6$ working lines in a block and tackle configuration, as illustrated in Figure A.1. Notice that there are $n_l + 1 = 7$ sheaves in the system, indexed from left to right with odd numbers on the crown block, and even numbers on the travelling block. Further, notice that the last sheave, $i = 7$ is stationary as the drill line on the right side is mounted to the anchor. Next, consider the last sheave at the travelling block, indexed $i = 6$. Since the previous sheave was stationary, the rotational velocity of this sheave is only depending on the translational velocity of the travelling block. Hence, the rotational velocity becomes $\omega_6 = -\frac{v_t}{r_s}$, where r_s is the radius of the sheave. The next sheave on the crown block is now rotating at the same rate as the previous sheave on the travelling block, but in the opposite direction. The same argumentation is valid for the next set of sheaves, but the velocity of the previous sheave must be added. One may

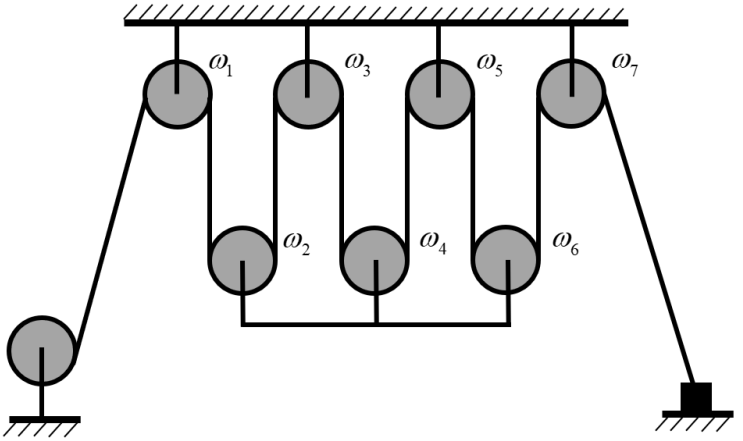

Figure A.1: Block and tackle system with a 6 working line configuration.

observe that for the specific configuration of $n_l = 6$, the angular velocities may be calculated as

$$\begin{aligned} \omega_1 &= 3\frac{v_t}{r_s}, & \omega_2 &= -3\frac{v_t}{r_s} \\ \omega_3 &= 2\frac{v_t}{r_s}, & \omega_4 &= -2\frac{v_t}{r_s} \\ \omega_5 &= \frac{v_t}{r_s}, & \omega_6 &= -\frac{v_t}{r_s} \\ \omega_7 &= 0, \end{aligned} \tag{A.1}$$

Now, by observing that $\omega_1 = 3\frac{v_t}{r_s} = \frac{n_l}{2}\frac{v_t}{r_s}$, one may use the following relationship to generalize the sheave velocities as functions of the first sheave.

$$\omega_1 = \frac{n_l v_t}{2r_s} \Longleftrightarrow \frac{v_t}{r_s} = \frac{2}{n_l}\omega_1 \tag{A.2}$$

Substituting this expression for $n_l = 6$ gives us the following velocities.

$$\begin{aligned} \omega_1 &= \omega_1, & \omega_2 &= -\omega_1 \\ \omega_3 &= \frac{2}{3}\omega_1, & \omega_4 &= -\frac{2}{3}\omega_1 \\ \omega_5 &= \frac{1}{3}\omega_1, & \omega_6 &= -\frac{1}{3}\omega_1 \end{aligned}$$

For this particular block and tackle configuration, the rotational velocity ratio for sheave $i \in \{1, 2, ..., 6\}$ becomes

$$\frac{\omega_i}{\omega_1} = \left\{1, -1, \frac{2}{3}, -\frac{2}{3}, \frac{1}{3}, -\frac{1}{3}\right\}. \tag{A.3}$$

For the purpose of finding an expression for this ratio for a given sheave i for an arbitrary n_l, the following relationship was found. For the sheaves on the travelling block, i.e. for i even, the following sequence emerged.

$$\frac{\omega_i}{\omega_1} = \left\{-1 + 0 \cdot \frac{2}{n_l}, -1 + 1 \cdot \frac{2}{n_l}, -1 + 2 \cdot \frac{2}{n_l} - 1 + 3 \cdot \frac{2}{n_l}, ..., -1 + k \cdot \frac{2}{n_l}\right\} \tag{A.4}$$

Similarly, for the sheaves on the crown block, i.e. for i odd, the following sequence emerged.

$$\frac{\omega_i}{\omega_1} = \left\{1 - 0 \cdot \frac{2}{n_l}, 1 - 1 \cdot \frac{2}{n_l}, 1 - 2 \cdot \frac{2}{n_l} 1 - 3 \cdot \frac{2}{n_l}, ..., 1 - k \cdot \frac{2}{n_l}\right\} \tag{A.5}$$

With these two sequences, the general ratio between the rotational velocity of sheave i and sheave 1 can be expressed as follows.

$$\frac{\omega_i}{\omega_1} = \begin{cases} -1 + \frac{2}{n_l}\left(\frac{i}{2} - 1\right), & \text{i even} \\ 1 - \frac{2}{n_l}\left(\frac{i+1}{2} - 1\right), & \text{i odd} \end{cases} \tag{A.6}$$

Thus concludes the sheave rotational velocity ratio derivation.

Appendix B

Derivation of the equations of motion

In this appendix, the equations of motion for the drawwork hoisting system will be derived based on the Lagrangian in Equation (2.49), restated here.

$$\begin{aligned}\mathcal{L} &= T - U \\ &= \frac{1}{2}J_{tot}\dot{\theta}_m^2 + \frac{1}{2}m_t\left(\gamma\dot{\theta}_m + \dot{z}_c\right)^2 + \frac{1}{2}m_c\dot{z}_c^2 \\ &- \frac{1}{2}k_c(z_{wt} - z_c)^2 - m_c g z_c - m_t g\left(\gamma\theta_m + (z_c - z_{wt})\right)\end{aligned} \tag{B.1}$$

In order to derive the equations of motion, this Lagrangian will be applied to the Lagrange's equation of motion, stated in Equation (2.31), restated here.

$$\frac{d}{dt}\left(\frac{\partial\mathcal{L}}{\partial\dot{q}_i}\right) - \frac{\partial\mathcal{L}}{\partial q_i} = \Xi_i \tag{B.2}$$

Here, q_i is the i$^{\text{th}}$ generalized coordinate in the model, and Ξ_i is the i$^{\text{th}}$ non-conservative force or torque. First, the equation of motion for the gen-

eralized coordinate θ_m will be calculated. The terms in Lagrange's equation of motion can be calculated separately, as follows.

$$\begin{aligned}
\frac{\partial \mathcal{L}}{\partial \dot{\theta}_m} &= J_{tot}\dot{\theta}_m + \gamma m_t(\gamma\dot{\theta}_m + \dot{z}_c) \\
&= \left(J_{tot} + \gamma^2 m_t\right)\dot{\theta}_m + \gamma m_t \dot{z}_c && \text{(B.3)} \\
\frac{d}{dt}\left(\frac{\partial \mathcal{L}}{\partial \dot{\theta}_m}\right) &= \left(J_{tot} + \gamma^2 m_t\right)\ddot{\theta}_m + \gamma m_t \ddot{z}_c && \text{(B.4)} \\
\frac{\partial \mathcal{L}}{\partial \theta_m} &= -\gamma m_t g && \text{(B.5)} \\
\Xi_{\theta_m} &= \tau_m - \tau_{hl} + \tau_{f,m} && \text{(B.6)}
\end{aligned}$$

Here, τ_m is the resulting torque from the motor expressed in Equation (2.8), τ_{hl} is the torque caused by hookload, and $\tau_{f,m}$ is the torque caused by friction, stated in Equation (2.27). Thus, the first equation of motion results in the following.

$$\left(J_{tot} + m_t\gamma^2\right)\ddot{\theta}_m + \gamma m_t \ddot{z}_c + \gamma m_t g = \tau_m - \tau_{hl} + \tau_{f,m} \qquad \text{(B.7)}$$

Next, the equation of motion for the generalized coordinate z_c will be calculated. Again, the terms in Lagrange's equation of motion will be stated separately.

$$\begin{aligned}
\frac{\partial \mathcal{L}}{\partial \dot{z}_c} &= m_t(\gamma\dot{\theta}_m + \dot{z}_c) + m_c\dot{z}_c \\
&= \gamma m_t\dot{\theta}_m + (m_t + m_c)\dot{z}_c && \text{(B.8)} \\
\frac{d}{dt}\left(\frac{\partial \mathcal{L}}{\partial \dot{z}_c}\right) &= \gamma m_t\ddot{\theta}_m + (m_t + m_c)\ddot{z}_c && \text{(B.9)} \\
\frac{\partial \mathcal{L}}{\partial z_c} &= k_c(z_{wt} - z_c) - (m_t + m_c)g && \text{(B.10)} \\
\Xi_{z_c} &= b_c(\dot{z}_{wt} - \dot{z}_c) - F_{hl} && \text{(B.11)}
\end{aligned}$$

The term $b_c(\dot{z}_c - \dot{z}_{wt})$ comes from the non-conservative damper force in the CMC, and F_{hl} is the hookload force, acting on the crown block. The second equation of motion results in the following.

$$\gamma m_t\ddot{\theta}_m + (m_t + m_c)\ddot{z}_c - k_c(z_{wt} - z_c) + (m_t + m_c)g = b_c(\dot{z}_{wt} - \dot{z}_c) - F_{hl} \tag{B.12}$$

Thus concludes the derivations of the equations of motion.

Appendix C

Merging the equations of motion

The equations of motion that are governing the dynamics in the hoisting system were derived in Chapter 2, and are stated as follows.

$$\frac{di_a}{dt} = \frac{1}{L_a}(u - K_v\omega_m - R_a i_a) \tag{C.1}$$

$$\tau_m = K_t i_a - B_a \omega_m \tag{C.2}$$

$$\left(J_{tot} + m_t\gamma^2\right)\ddot{\theta}_m + \gamma m_t \ddot{z}_c + \gamma m_t g = \tau_m - \tau_{hl} + \tau_{f,m} \tag{C.3}$$

$$\gamma m_t \ddot{\theta}_m + (m_t + m_c)\ddot{z}_c - k_c(z_{wt} - z_c) + (m_t + m_c)g = b_c(\dot{z}_{wt} - \dot{z}_c) - F_{hl} \tag{C.4}$$

For the purpose of simplifying the control system derivations, merging these equations into one equation of motion will be beneficial. In order to do so, the equations will be transformed into the Laplace domain for simpler calculations. Consider Equation (C.1) in the Laplace domain.

$$i_a s = \frac{1}{L_a}(u - K_v\omega_m - R_a i_a) \tag{C.5}$$

Sorting the terms, and solving for i_a yields

$$i_a = \frac{1}{L_a s + R_a} u - \frac{K_v}{L_a s + R_a} \omega_m \tag{C.6}$$

which may be substituted into Equation (C.2), resulting in a torque equation without motor current dependencies,

$$\tau_m = \frac{K_t}{L_a s + R_a} u - \left(\frac{K_v K_t}{L_a s + R_a} + B_a \right) \omega_m. \tag{C.7}$$

Next, the Equations (C.3) and (C.4) will be merged by eliminating the crown block acceleration term $\ddot{z}_c$. Consider Equation (C.4), solved for $\ddot{z}_c$.

$$\ddot{z}_c = \frac{1}{m_t + m_c} \left(b_c(\dot{z}_{wt} - \dot{z}_c) - F_{hl} - (m_t + m_c)g + k_c(z_{wt} - z_c) - \gamma m_t \ddot{\theta}_m \right) \tag{C.8}$$

This expression for the crown block acceleration will be substituted into Equation (C.3), yielding

$$\begin{aligned} \frac{\gamma m_t}{m_t + m_c} \left(b_c(\dot{z}_{wt} - \dot{z}_c) - F_{hl} - (m_t + m_c)g + k_c(z_{wt} - z_c) - \gamma m_t \ddot{\theta}_m \right) \\ + \left(J_{tot} + m_t \gamma^2 \right) \ddot{\theta}_m + \gamma m_t g = \tau_m - \tau_{hl} + \tau_{f,m}. \end{aligned} \tag{C.9}$$

Substituting γF_{hl} for τ_{hl}, and sorting the terms yields the following expression.

$$\begin{aligned} \left[J_{tot} + \gamma^2 m_t \left(1 - \frac{m_t}{m_t + m_c} \right) \right] \ddot{\theta}_m = \\ \tau_m - \left(1 - \frac{m_t}{m_t + m_c} \right) \tau_{hl} + \tau_{f,m} - \frac{\gamma m_t}{m_t + m_c} \left(k_c(z_{wt} - z_c) + b_c(\dot{z}_{wt} - \dot{z}_c) \right) \end{aligned} \tag{C.10}$$

By Laplace transforming this expression, and substituting for the motor torque in Equation (C.7), results in the final expression.

$$\left[\left(J_{tot} + m_t\gamma^2\left(1 - \frac{m_t}{m_t + m_c}\right)\right)s^2 + \left(\frac{K_v K_t}{L_a s + R_a} + B_a\right)s\right]\theta_m = \frac{K_t}{L_a s + R_a}u - \left(1 - \frac{m_t}{m_t + m_c}\right)\tau_{hl} + \tau_{f,m} - \frac{m_t\gamma}{m_t + m_c}(k_c + b_c s)(z_{wt} - z_c) \tag{C.11}$$

Thus concludes the merging of the equations of motion.

Morten Lie

Heave Compensated Tripping

NTNU
Norwegian University of
Science and Technology